JGR Space Physics

RESEARCH ARTICLE
10.1029/2020JA028224

Key Points:
- Thermospheric temperature enhancement and inversion layer detected by lidar in Antarctica was reproduced in TIEGCM with modified drivers
- Regional-scale aurora and subgrid E field variability are both important to produce realistic storm-time neutral temperatures and densities
- Differential heating by intense Joule heating at ~120 km and adiabatic cooling above, plus vertical advection, generate the TTEIL in model

Supporting Information:
- Supporting Information S1

Correspondence to:
X. Lu and H. Wu,
xianl@clemson.edu;
haonanw@clemson.edu

Citation:
Wu, H., Lu, X., Lu, G., Chu, X., Wang, W., Yu, Z., et al. (2020). Importance of regional-scale auroral precipitation and electrical field variability to the storm-time thermospheric temperature enhancement and inversion layer (TTEIL) in the Antarctic E region. *Journal of Geophysical Research: Space Physics*, *125*, e2020JA028224. https://doi.org/10.1029/2020JA028224

Received 11 MAY 2020
Accepted 20 AUG 2020
Accepted article online 24 AUG 2020

Importance of Regional-Scale Auroral Precipitation and Electrical Field Variability to the Storm-Time Thermospheric Temperature Enhancement and Inversion Layer (TTEIL) in the Antarctic E Region

Haonan Wu[1], Xian Lu[1], Gang Lu[2], Xinzhao Chu[3,4], Wenbin Wang[2], Zhibin Yu[5], Liam M. Kilcommons[4], Delores J. Knipp[2,4], Boyi Wang[6], and Yukitoshi Nishimura[7]

[1]Department of Physics and Astronomy, Clemson University, Clemson, SC, USA, [2]High Altitude Observatory, National Center for Atmospheric Research, Boulder, CO, USA, [3]Cooperative Institute for Research in Environmental Sciences, University of Colorado, Boulder, CO, USA, [4]Smead Department of Aerospace Engineering Sciences, University of Colorado, Boulder, CO, USA, [5]Institute of Space Science and Applied Technology, Harbin Institute of Technology, Shenzhen, China, [6]Geophysical Institute, University of Alaska, Fairbanks, AK, USA, [7]College of Electrical and Computer Engineering, Boston University, Boston, MA, USA

Abstract A dramatic thermospheric temperature enhancement and inversion layer (TTEIL) was observed by the Fe Boltzmann lidar at McMurdo, Antarctica during a geomagnetic storm Chu et al. (2011); https://doi.org/10.1029/2011GL050016). The Thermosphere-Ionosphere-Electrodynamics General Circulation Model (TIEGCM) driven by empirical auroral precipitation and background electric fields cannot adequately reproduce the TTEIL. We incorporate the Defense Meteorological Satellite Program (DMSP)/Special Sensor Ultraviolet Spectrographic Imager (SSUSI) auroral precipitation maps, which capture the regional-scale features into TIEGCM and add subgrid electric field variability in the regions with strong auroral activity. These modifications enable the simulation of neutral temperatures closer to lidar observations and neutral densities closer to GRACE satellite observations (~475 km). The regional scale auroral precipitation and electric field variabilities are both needed to generate strong Joule heating that peaks around 120 km. The resulting temperature increase leads to the change of pressure gradients, thus inducing a horizontal divergence of air flow and large upward winds that increase with altitude. Associated with the upwelling wind is the adiabatic cooling gradually increasing with altitude and peaking at ~200 km. The intense Joule heating around 120 km and strong cooling above result in differential heating that produces a sharp TTEIL. However, vertical heat advection broadens the TTEIL and raises the temperature peak from ~120 to ~150 km, causing simulations deviating from observations. Strong local Joule heating also excites traveling atmospheric disturbances that carry the TTEIL signatures to other regions. Our study suggests the importance of including fine-structure auroral precipitation and subgrid electric field variability in the modeling of storm-time ionosphere-thermosphere responses.

1. Introduction

Magnetospheric energy is dissipated in the ionosphere-thermosphere (I-T) region through Joule heating and particle precipitation (Cole, 1975). Most of energy from the convergence of Poynting flux results in Joule heating (Knipp et al., 2004; Richmond & Thayer, 2000; Thayer et al., 1995; Thayer & Semeter, 2004), while auroral particle precipitation heats the atmosphere directly through collision and indirectly by increasing conductivity and thus Joule heating. The frictional collisions between ions and neutrals cause temperature enhancement and subsequent pressure divergence, leading to upward neutral motions. Furthermore, Lorentz force accelerates neutrals by transferring momentum from fast-moving ions (Mikkelsen et al., 1981). During periods of strong geomagnetic activity, both auroral precipitation and electric fields are elevated, leading to enhanced energy deposition in the I-T region (e.g., Deng et al., 2011; Fuller-Rowell et al., 1987; Heppner et al., 1993; Wang et al., 2005). For instance, the localized extreme Poynting flux has been detected to exceed 170 mW/m^2 by the Defense Meteorological Satellite Program (DMSP) spacecraft with substantial temporal and spatial variability in the auroral zone (Knipp et al., 2011). Although the Weimer statistical

model (Weimer, 2005) predicts a peak Joule heating rate of 15 mW/m^2, satellite observations have revealed that the localized Earth-directed Poynting fluxes can be several times larger during magnetic storms (Huang et al., 2016; Huang & Burke, 2004).

Such localized energy deposition and its effects, however, are difficult to capture in the I-T models driven by empirical high-latitude inputs because those drivers are usually obtained from statistical auroral maps (e.g., Hardy et al., 1985; Newell et al., 2009) and electric convection patterns (e.g., Heelis et al., 1982; Weimer, 2005). The statistical auroral maps usually miss localized features in the resolved grids, and convection patterns usually miss subgrid temporal and spatial variabilities (Cosgrove et al., 2011; Matsuo & Richmond, 2008). To reduce the gap between observations and statistical models, data assimilation methods such as Assimilative Mapping of Ionospheric Electrodynamics (AMIE) (Richmond, 1992; Richmond & Kamide, 1988) have been developed to synthesize available observations into coherent patterns to provide more realistic electric fields. However, even with data assimilation techniques, comparisons of the AMIE outputs with the direct observations still show significant discrepancies (Cosgrove et al., 2009; Cosgrove & Codrescu, 2009).

It has been shown that electric field variability has a comparable contribution to Joule heating as the mean electric field (Codrescu et al., 2000), and therefore, omitting electric field variability causes a significant underestimation of Joule heating in the models (Codrescu et al., 1995, 2008; Deng et al., 2009; Matsuo & Richmond, 2008). Since Joule heating is the overall dominant heating source in the polar region during storm times, the underestimation of Joule heating leads to an underestimated global heating budget, which further influences the calculation of global circulation. Emery et al., (1999) introduced a parameterized way of accounting for the missing contribution from subgrid electric field variabilities in Thermosphere Ionosphere Electrodynamics General Circulation Model (TIEGCM) by multiplying Joule heating by a factor of 1.5 globally, which effectively increases the global Joule heating budget to a reasonable level but neglects the spatial distribution of electric field variabilities. Satellite and ground-based observations have found that large electric field variabilities occur mainly in the auroral zone (Cousins & Shepherd, 2012a, 2012b; Matsuo et al., 2003). By analyzing plasma drift measurements obtained from the Dynamic Explorer 2 (DE-2) mission, Matsuo et al., (2003) found that the electric field variability exceeds the magnitude of the mean electric field in the polar area. Cousins and Shepherd (2012a) statistically studied small-scale electric field variabilities on spatial scales between 45 and 450 km and temporal scales between 2 and 20 min using 4 years of Super Dual Auroral Radar Network (SuperDARN) line-of-sight ion drift measurements. They found that the small-scale variability shows spatial distribution that is correlated with the gradient in the background plasma drift, likely originating from small-scale magnetospheric turbulences. Note that the mean spatial scale they studied (~225 km) is comparable to the typical resolution of I-T models. Cousins and Shepherd (2012b) further examined the distribution of electric field temporal and spatial variabilities, which are found to peak in the auroral region under negative interplanetary magnetic field (IMF) B_z and in winter times.

The motivation of this work originates from the large neutral thermospheric temperature elevation in the E region altitude detected by an iron (Fe) Boltzmann lidar (Chu et al., 2002) at McMurdo (77.8°S, 166.7°E), Antarctica around 15 universal time (UT) during the 28 May 2011 storm event (Figure 2c in Chu et al., 2011, replotted as Figure 1a in this paper). The storm resulted from passage of two interplanetary coronal mass ejections (ICMEs), both with clear magnetic cloud signatures (Chi et al., 2018), and was accompanied by strong aurora activity as shown in the auroral electrojet (AE) index. The IMF B_z southward fields from the ICMEs joined in an interaction region that passed Earth from ~1,300 to 1,430 UT. The IMF B_z was southward from 0600 to 1500 in UT during which the planetary K (Kp) index was 6 and symmetric disturbances of the horizontal geomagnetic field (SYM-H) index dropped to about 100 nT (Figures 1b–1e). Compared to the Naval Research Laboratory Mass Spectrometer and Incoherent Scatter Radar (NRLMSISE-00) model (Picone et al., 2002), the storm-time neutral temperature profile was dramatically elevated with a maximum increase of ~550 K at ~134 km (Chu et al., 2011). This leads to a local temperature peak in altitude and the formation of a neutral thermospheric temperature enhancement and inversion layer (TTEIL) at E region altitudes, defined as the structure showing temperature increase and then decrease with altitude.

Most of the storm studies have been dedicated to investigating the responses of ionospheric parameters such as ion drifts and electron densities (e.g., Lu et al., 2008; Lu, Pi, et al., 1998) or neutral density and wind variations in the upper thermosphere (e.g., Forbes et al., 2005; Lei et al., 2010; Sutton et al., 2005). A few studies

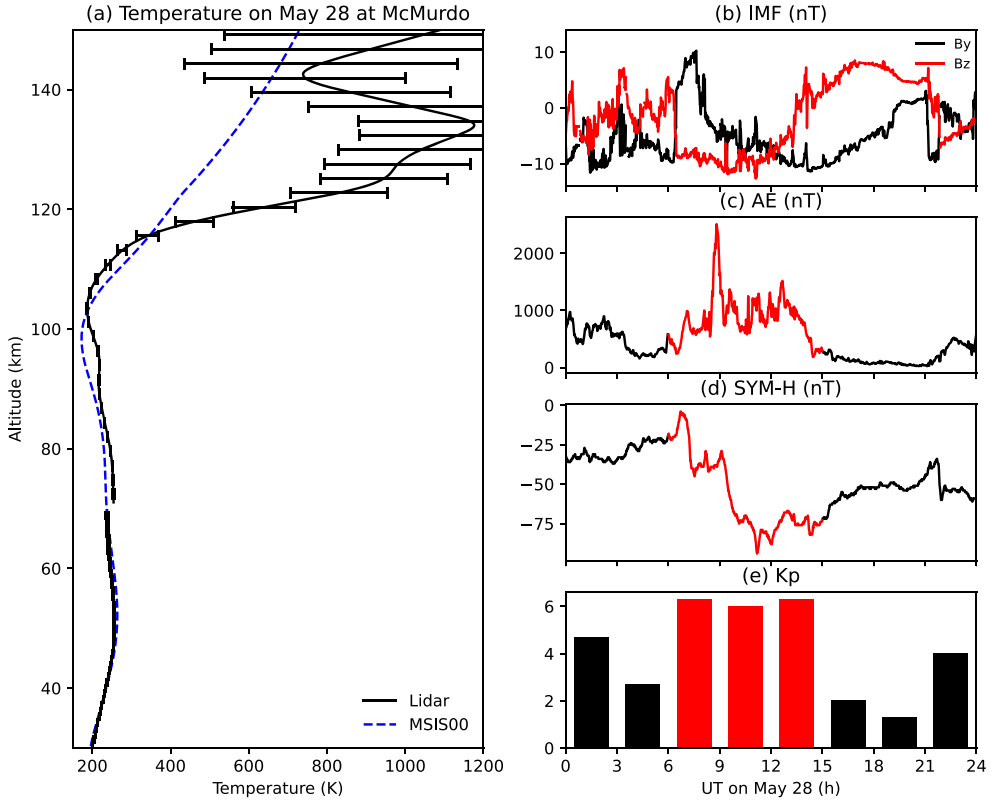

Figure 1. (a) The vertical profile of temperatures for 1 hr integration around 15 UT measured by the lidar (replotted from Figure 2c in Chu et al., 2011). (b–e) Geomagnetic indices showing IMF, AE, SYM-H, and Kp, respectively, on 28 May 2011.

have reported the storm effects on neutral temperatures in the mesosphere and lower thermosphere which cause perturbation of tens of Kelvin (Fagundes et al., 1996; Laštovička, 1996; Liu et al., 2018; Li et al., 2018; Li, Wang, et al., 2019; Yuan et al., 2015). It is intriguing that such tremendous neutral temperature elevation is present at E region altitudes (110–150 km) with an associated inversion layer. Furthermore, another event with a similar temperature enhancement and inversion layer, but somewhat a smaller magnitude was observed by the same Fe Boltzmann lidar at McMurdo on 2 May 2011 (Chu et al., 2011). Therefore, such thermospheric enhancement and inversion at E region altitudes may not be rare in the neutral atmospheric responses to storms. On the other hand, even though the I-T models with statistical high-latitude drivers provide fair predictions of the medium- and large-scale storm-time dynamics in the upper atmosphere, none of them can simulate the TTEIL seen in the local lidar observations, which challenges our understanding and modeling of the magnetosphere-ionosphere-thermosphere (MIT) coupling processes. To investigate these features, we implement the auroral precipitation maps from Special Sensor Ultraviolet Spectrographic Imager (SSUSI) observations onboard the DMSP satellites and incorporate the electric field variability into the TIEGCM (section 2). The model outputs are compared with neutral temperatures observed by the lidar and neutral density measurements from the Gravity Recovery and Climate Experiment (GRACE) satellite. By pushing the simulation closer to observations, we aim to investigate the generation mechanism of TTEIL in the model, the sources of local heating and cooling, and the neutral dynamics effects (section 3). Additional modeling efforts to simulate the TTEIL and the limitations of this work are discussed in section 4.

2. Model, Data, and Methodology

2.1. Model Setup

In this study, the TIEGCM version 2.0 which has a horizontal resolution of 2.5° in latitude and longitude and a vertical resolution of ¼ scale height is used. TIEGCM is a global 3-D numerical model that simulates the

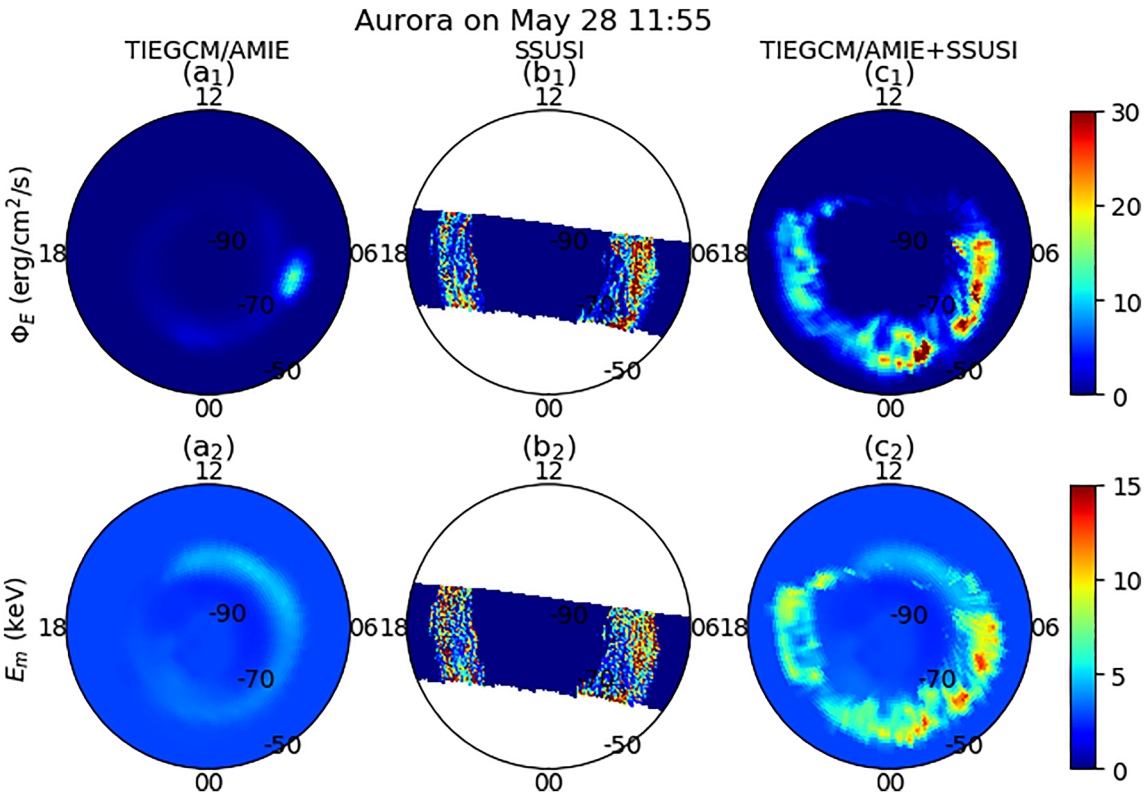

Figure 2. (a_1–c_1) aurora maps of Φ_E from TIEGCM/AMIE (a_1), SSUSI (b_1), and a combined map of TIEGCM/AMIE and SSUSI (c_1). The plotting time is 11:55 UT for (a_1) and (c_1) and 11:42–12:05 UT for (b_1). (a_2–c_2) are the same except for E_m. All plots are in magnetic latitude—magnetic local time coordinates.

coupled thermosphere/ionosphere system from ~97 to ~600 km altitude. It self-consistently solves the fully coupled, nonlinear, hydrodynamic, thermodynamic, and continuity equations of the neutral gas, the ion and electron energy equations, the O^+ continuity equation and ion chemistry, and the neutral wind dynamo (Qian et al., 2014; Richmond, 1995; Richmond et al., 1992; Roble et al., 1987, 1988). The lower boundary tides are derived from a linear atmospheric model assimilated with Sounding of the Atmosphere using Broadband Emission Radiometry (SABER) and Thermosphere-Ionosphere-Mesosphere Energetics and Dynamics (TIMED) Doppler Interferometer (TIDI) observations (Wu et al., 2012; Yamazaki et al., 2014). The time step of TIEGCM simulation is 30 s. Diagnostic outputs are saved every minute.

One of the important high-latitude drivers for the I-T model is the electric field (or electric potential) mapped down from the magnetosphere. AMIE is designed to assimilate observational data from various sources to provide more realistic high-latitude electric field convection pattern (Knipp et al., 1993; Lu et al., 1995; Ridley et al., 1998), which is used in this study to drive TIEGCM. The data assimilated in AMIE for this event include magnetic field perturbations from 265 ground-based magnetometers (197 in Northern Hemisphere, 68 in Southern Hemisphere) through the SuperMAG network (Gjerloev, 2009, 2012) and from the Iridium satellite magnetometers through the Active Magnetosphere and Planetary Electrodynamics Response Experiment (AMPERE) project (Anderson et al., 2008, 2014). The line-of-sight ion drifts from SuperDARN (Chisham et al., 2007; Greenwald et al., 1995) and auroral particle precipitation measured by the Special Sensor J (SSJ) instrument onboard the DMSP F16, F17, and F18 satellites (Kadinsky-Cade et al., 2004) are also used.

2.2. Incorporating DMSP/SSUSI Observations Into TIEGCM Auroral Precipitation Maps

Another high-latitude driver for the TIEGCM is auroral precipitation, which is also obtained through the AMIE fitting procedure. Assuming Maxwellian distributions, auroral precipitation can be described by two key parameters: mean energy (E_m) and energy flux (Φ_E) (Rees & Luckey, 1974; Robinson & Vondrak, 1985; Roble & Ridley, 1987). E_m and Φ_E in TIEGCM/AMIE describe the enhancement of aurora during storm times, but underestimation of auroral activity still exists. Figure 2 shows an example of the

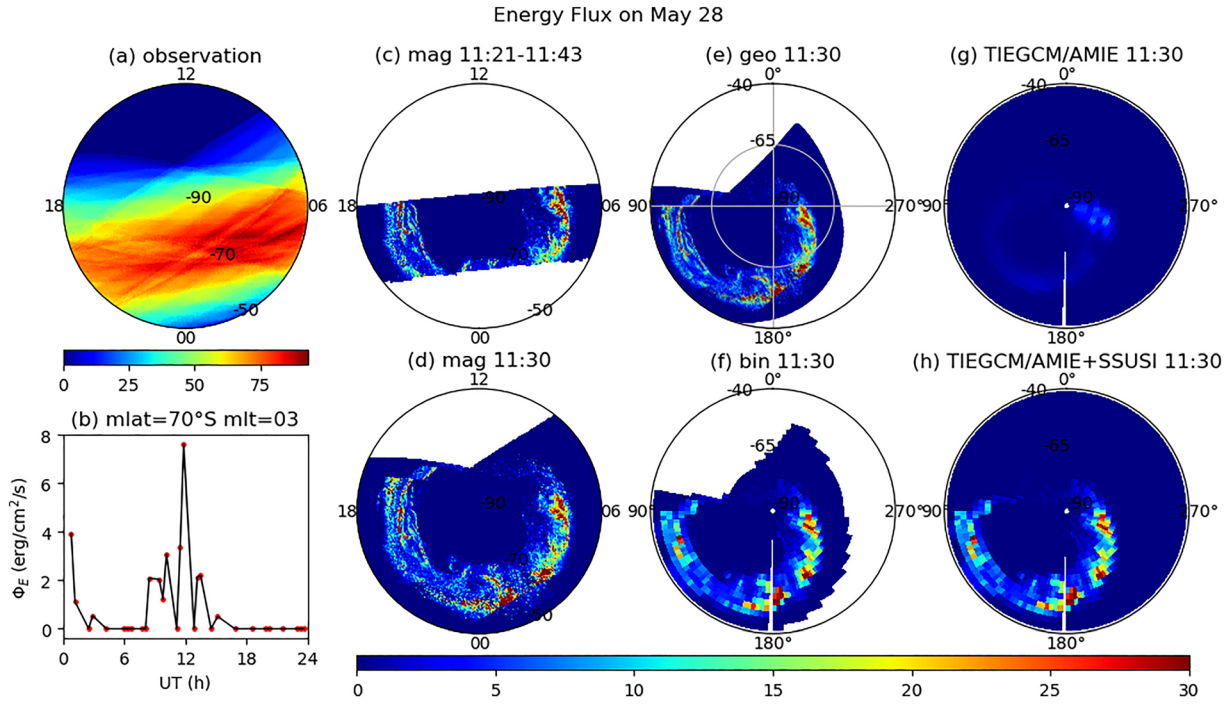

Figure 3. (a) Total sampling numbers for the satellite auroral observations measured by SSUSI from DMSP F16, F17, and F18 from 27 to 29 May, in magnetic latitude/local time coordinate. (b) Linear interpolation of energy flux (Φ_E) at 70°S magnetic latitude and 3 magnetic local time. Red dots are observations and black line corresponds to the interpolated results with a time interval of 30 s. (c) Raw Φ_E from 11:21 to 11:43 UT in magnetic latitude/local time coordinate. (d) Φ_E after temporal interpolation and projected to 11:30 UT. (e) Φ_E in geographic coordinates after coordinate transformation. (f) Φ_E in geographic coordinates after binning to TIEGCM grids (2.5° in latitude and longitude). (g) Original Φ_E maps of TIEGCM/AMIE. (h) Φ_E in TIEGCM after combining AMIE and SSUSI.

comparisons of Φ_E and E_m between TIEGCM/AMIE and DMSP/SSUSI observations around 11:55 UT. Comparing Figures $2a_1$ and $2a_2$ with $2b_1$ and $2b_2$, the position of the auroral oval is reasonably captured, but its magnitude is significantly underestimated and regional structures are not resolved.

To mitigate the underestimation of auroral precipitation in TIEGCM for this study, we modify the aurora maps in TIEGCM according to SSUSI observations. We use the auroral Environmental Data Record (EDR) data (Paxton et al., 1992), which contain Φ_E and E_m derived from the observed spectral intensities. For the 28 May event, three DMSP satellites (F16, F17, and F18) were taking measurements, and therefore, they are all used. The raw Φ_E and E_m data of each swath are provided in 2-D magnetic latitude/local time grids with extremely fine resolution (~0.1° magnetic latitude × ~ 0.01 hr magnetic local time). The number of data samplings from all three satellites over each magnetic latitude/local time grid for the time period of 27–29 May is shown in Figure 3a. This polar map indicates the coverage of satellite observations. The satellites passed most of the region on the night side for more than 70 times, while missing the dayside sector to a large extent. To take the advantage of the available observations and fill up the observational gaps, we combine observations and the model as follows:

1. We collect SSUSI observations from all three satellites falling into each magnetic latitude/local time grid to form a time series with respect to UT, which is unevenly distributed. The red dots in Figure 3b show Φ_E measured by SSUSI on 28 May at 70°S magnetic latitude (MLAT) and 03 magnetic local time (MLT). We apply linear temporal interpolation in UT to project the data into an evenly distributed time series with a time interval of 30 s to be used by the model (black line in Figure 3b). Figure 3c shows the original Φ_E observations from one satellite pass between 11:21 and 11:43 UT, and Figure 3d shows the temporally interpolated Φ_E at 11:30 UT, which is obtained through interpolation from multiple satellite passes. Most of the polar areas are covered except for the dayside sector, where the satellites have no passes. When temporal interpolation happens at a time (e.g., 11:30 UT as in Figure 3d) close to the time when the observation is taken (e.g., 11:21–11:43 UT shown in Figure 3c), the interpolated aurora (Figure 3d) tends to approach the observation (Figure 3c) due to the proximity in time.

2. After the linear interpolation, the auroral maps are converted from geomagnetic latitude/local time coordinates to geographic latitude/longitude coordinates (Figure 3e), which are nonuniform spatially after the conversion and have a finer spatial resolution than the TIEGCM. To obtain aurora maps on the regular TIEGCM grids, spatial binning is performed on the geographic coordinate by taking the average of the 20–30 points falling into each model grid (Figure 3f), which includes both the real SSUSI observations and the interpolated results. The standard deviations of these points are also calculated and retained for mechanism studies (section 3.1). This binning operation is performed at every interpolating time step (30 s).
3. We replace the TIEGCM/AMIE auroral maps with the temporally interpolated and spatially binned SSUSI maps obtained after step 2 wherever available. For the regions where satellites do not pass (such as the dayside sector in the polar map), we use the auroral maps from the model (TIEGCM/AMIE), which usually occupies ~20% of the overall auroral region. Using the model maps is a reasonable approximation considering that auroral activity in the dayside sector is generally weak (e.g., Newell et al., 2009), thus the differences between observations and model are relatively small.

The combined TIEGCM/AMIE and SSUSI maps are shown in Figures 3h, $2c_1$, and $2c_2$, which are referred to as "SSUSI-modified" auroral maps. These maps are generated every 30 s and used as inputs to drive TIEGCM. Comparing Figures 3g with 3h, $2a_1$ with $2c_1$, and $2a_2$ with $2c_2$, the overall position of the auroral oval is well represented in the default model maps, while the magnitudes of Φ_E and E_m are enhanced significantly and show regional-scale structures in the modified auroral precipitation. The combination of the observed and default auroral maps is susceptible to discontinuity at their boundaries (Figure 3h). We have performed sensitivity tests to the boundary being smoothed by taking the running mean of the adjacent 9 grid points, and the results do not show noticeable differences from the runs we present here.

It should be noted that for any particular geophysical location where the SSUSI-interpolated-binned map (Step 3) is available, real-time observations are still sparse, so most data points are from the temporal interpolation (Figure 3b). Even so, since the real-time continuous observations covering the whole auroral regions are not available, the temporal interpolation is one of the simplest realizations of the aurora variations that takes advantage of real data information for this particular storm event. It also helps maintain the regional structure of aurora. As will be shown in section 3, the auroral modification improves the simulation of neutral temperatures and densities in general.

2.3. Implementing Subgrid Scale Electric Field Variability

To account for the effects of subgrid scale electric field variabilities and their nonuniform spatial distribution, we change the Joule heating factor from 1.5 used in the default TIEGCM runs (Emery et al., 1999) to 1 in all of our runs and introduce the variability by adding a random number (E') to the resolved electric field (E_0) obtained from the AMIE procedure at each time step. This is similar to the procedure conducted in Matsuo and Richmond (2008), which treated the subgrid variability as a stochastic process and simulated it as random numbers in numerical modeling. Cousins and Shepherd (2012a) derived the statistical distribution of small-scale electric field variabilities, which follow a two-sided exponential distribution ($e^{-|E'|/\mu}$) instead of Gaussian (also seen in Golovchanskaya et al., 2006), where E' is the electric field fluctuation and μ is the characteristic electric field variability. Cousins and Shepherd (2012b) found that the ratios of μ to the background electric field are large in the auroral zone (often close to 1) and small in other regions. Following their work, we choose the random number (E') from an exponential distribution $e^{-|E'|/\mu}$ with μ equal to the local resolved electric field (E_0) as the proxy of electric field variability. To correlate the variabilities to the spatial distribution of the auroral zone, they are added only in the strong auroral precipitation regions where Φ_E is over a threshold of $\Phi_{E0} = 5$ erg/cm^2/s, that is,

$$\frac{\mu(t)}{E_0(t)} = \begin{cases} 0, \Phi_E < \Phi_{E0} \\ 1, \Phi_E > \Phi_{E0} \end{cases} \quad (1)$$

And the overall electric field adopted in the model is $E(t) = E_0(t) + E'(t)$. The ratio μ/E_0 and threshold Φ_{E0} are also adjusted by checking the temperature responses. In general, a larger μ/E_0 and a smaller Φ_{E0} lead to a larger temperature enhancement. A smaller threshold Φ_{E0} value leads to a larger area where the implementation of adding electric field variability is applied; a larger μ/E_0 ratio means that for the regions where

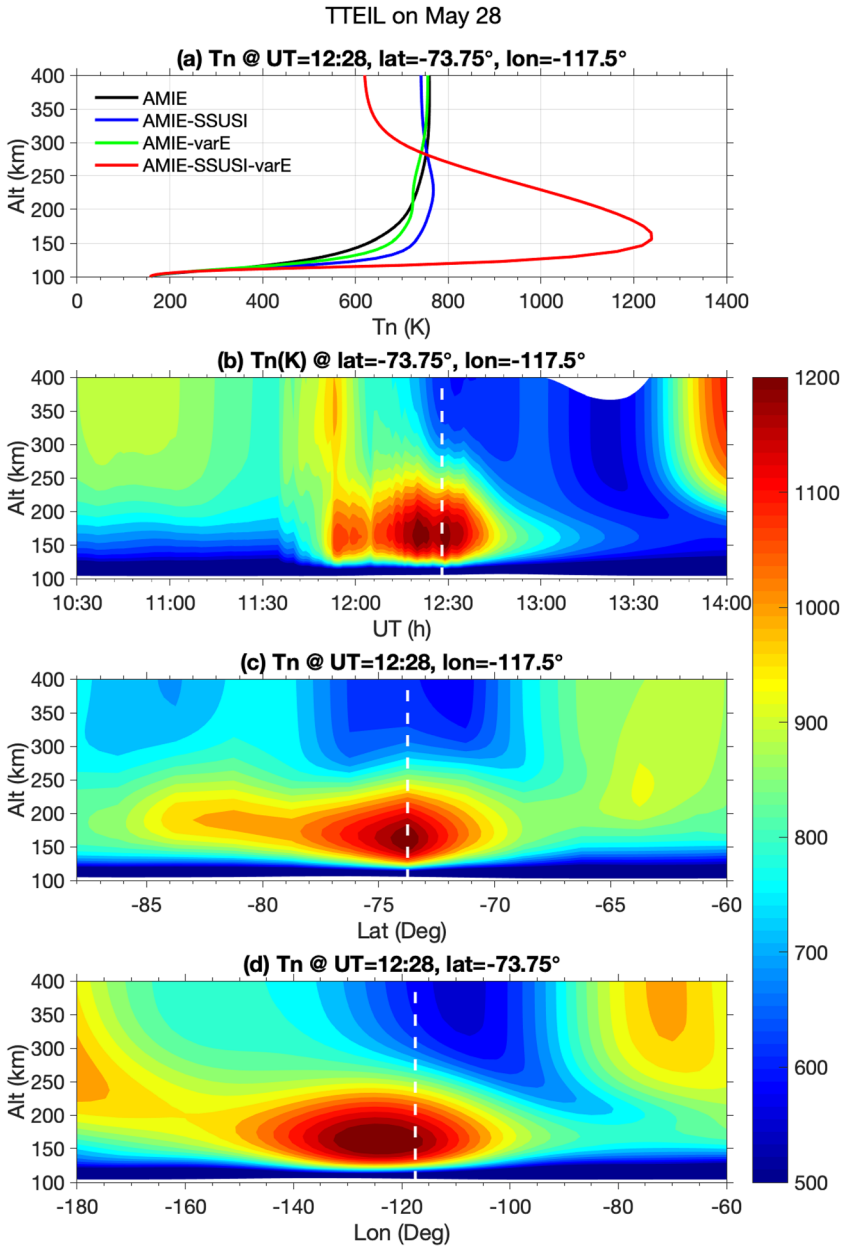

Figure 4. (a) Vertical temperature profiles at (73.75°S, 117.5°W) and 12:28 UT from four different TIEGCM runs indicated by different colors. (b–d) TTEIL structures from Run 4 with respect to, geographic latitude and longitude. White dashed lines highlight the time and location for the vertical profile shown in (a).

electric field variabilities are added, the magnitudes of the variabilities are larger. We choose the numbers that best reproduce the neutral density and temperature observations while maintaining numerical stability.

3. Mechanism Studies of the Strong TTEIL

Mechanism studies are conducted in two major steps. The first step covers auroral regions (sections 3.1–3.4), and the second step focuses on a local region around McMurdo (section 3.5).

3.1. Neutral Temperature Structures and Simulated TTEIL

In compliance with the modifications introduced in sections 2.2 and 2.3, four sets of TIEGCM runs with different configurations of the two high-latitude drivers are designed and named as follows:

Run 1(AMIE)	use AMIE electric potential and auroral maps (control run).
Run 2 (AMIE_SSUSI)	use AMIE electric potential, and SSUSI-modified auroral maps.
Run 3 (AMIE_varE)	use AMIE electric potential and auroral maps, but add electric field variabilities in the auroral region according to SSUSI-modified auroral maps.
Run 4 (AMIE_SSUSI_varE)	use AMIE electric potential, SSUSI-modified auroral maps, and add electric field variabilities according to SSUSI-modified auroral maps.

Figure 4a reveals the vertical profiles of neutral temperatures when and where the largest temperature increase and a strong TTEIL are located (73.75°S, 117.5°W). We refer this as the "primary TTEIL" to differentiate from the relatively weak ones generated by different mechanisms (to be discussed in sections 3.3 and 3.5). Compared with Run 1 (black line), only Run 4 (red line) produces a large temperature increase (~600 K at ~150 km) and a prominent TTEIL, while the magnitudes of the temperature increase from Runs 2 and 3 are much smaller. The comparisons of these neutral temperature profiles imply that both the enhanced auroral precipitation which increases ionization rates and the electric field variabilities play important roles in elevating the temperatures at ~150 km and forming the TTEIL.

As described in section 2.2, the standard deviations of auroral precipitation in terms of Φ_E and E_m are calculated and stored. We incorporate the variability of auroral precipitation into the model using the same method as that for the electric field except that the random numbers follow Gaussian distribution. The model tests (not shown here) of adding subgrid aurora variability show similar vertical structure of neutral temperatures as the runs without adding it, which suggests that the impact of aurora precipitation variability is minor when compared with the precipitation itself. This is expected since Joule heating is linearly related to Pedersen conductivity determined by precipitation, so the precipitation variability is likely to be smoothed out with time and space leading to a minimal net effect to the Joule heating budget (Lu, Baker, et al., 1998).

We focus on Run 4 to demonstrate the temporal and spatial structures of TTEIL (Figures 4b–4d). The horizontal red stripe around 100–200 km from 11:50 to 12:50 UT indicates that the simulated TTEIL lasts for ~1 hr. Starting from 11:40 UT, neutral temperature enhancement is present above 120 km. After 12:00 UT, neutral temperature above 200 km starts to decrease but the enhancement between 120 and 200 km lasts, which increases the contrast of temperatures between ~150 km and above, strengthening the magnitude of TTEIL. The TTEIL magnitude is defined as the temperature difference between the maximum temperature identified in the vertical range of 100–200 km and the minimum temperature above this maximum temperature peak. We choose the time of 12:28 UT when TTEIL reaches its maximum to examine its spatial extension (Figures 4c and 4d). The latitudinal and longitudinal spans of TTEIL are ~20° and ~80°, indicating that TTEIL is a large-scale phenomenon.

3.2. Thermodynamic Term Analysis and TTEIL Formation Mechanism

TIEGCM calculates neutral temperature by solving the thermodynamic equation in the dimensionless log-pressure coordinate z (=ln p_0/p) with the form

$$\frac{\partial T}{\partial t}=\frac{ge^z}{p_0C_p}\frac{\partial}{\partial z}\left[\frac{K_T}{H}\frac{\partial T}{\partial z}+K_EH^2C_p\rho\left(\frac{g}{C_p}+\frac{1}{H}\frac{\partial T}{\partial z}\right)\right]-\boldsymbol{v}\cdot\nabla T-ww\left(\frac{\partial T}{\partial z}+\frac{R^*T}{C_pm}\right)+\frac{Q-e^zL_e}{C_p}-L_iT \quad (2)$$

where T = neutral temperature, g = gravity constant, p_0 = reference pressure, C_p = heat capacity in constant pressure, K_T = heat conduction coefficient, H = scale height, K_E = eddy diffusion coefficient, ρ = neutral density, $\mathbf{v}$ = horizontal neutral wind vector, w = vertical neutral wind = dz/dt, R^* = universal gas constant, $\overline{m}$ = mean molar mass, Q = other diabatic heating except for heat conduction and eddy diffusion, L_e, L_i = diabatic cooling coefficients.

The heating terms on the right-hand side (RHS) of Equation 2 are grouped into six categories:

$\frac{ge^z}{p_0C_p}\frac{\partial}{\partial z}\left(\frac{K_T}{H}\frac{\partial T}{\partial z}\right)$	heat conduction (Q_C).
$\frac{ge^z}{p_0C_p}\frac{\partial}{\partial z}\left[K_EH^2C_p\rho\left(\frac{g}{C_p}+\frac{1}{H}\frac{\partial T}{\partial z}\right)\right]$	vertical heat transfer by eddy diffusion.
$-\boldsymbol{v}\cdot\nabla T$	horizontal heat advection (Q_H).

$w\frac{\partial T}{\partial z}$ vertical heat advection (Q_V).

$w\frac{R^* T}{C_p \overline{m}}$ adiabatic cooling (Q_A).

$\frac{Q}{C_p}$ diabatic heating, including Joule heating (Q_J), particle precipitation, solar, and chemical heating.

$\frac{e^z L_e}{C_p} \quad L_i T$ diabatic cooling.

All parameters on the RHS of Equation 2 are outputs from the model simulation and retrieved every minute, as are their individual contributions to time rate of temperature change ∂T/∂t. Figure 5 reveals ∂T/∂t induced by Joule heating (Q_J), adiabatic cooling (Q_A), vertical heat advection (Q_V), horizontal heat advection (Q_H), and heat conduction (Q_C) at (73.75°S, 117.5°W). At this location, Joule heating is the most significant term among all the diabatic heating terms when the TTEIL is generated. Other diabatic heating/cooling terms in TIEGCM including solar radiative heating and heating due to oxygen recombination, heat transfer by molecular diffusion, and diabatic cooling (such as NO and O^{3p} radiative cooling) are at least 1 order of magnitude smaller than the major terms in the altitude of 100–200 km, which are thus ignored in the term analysis. In the long-term time scale sometimes extending to the recovery phase of storms, the radiative cooling such as NO cooling is large and important to the overall energy budget (e.g., Knipp et al., 2017; Lei et al., 2011; Li, Knipp, & Wang, 2019; Lu et al., 2010).

Since Joule heating results from external driving (magnetospheric perturbation) and is related to electrodynamic processes, it appears much more sporadically (Figure 5a) than other heating/cooling terms which involve neutral motion and requires more inertia to change. Joule heating penetrates all the way down to ~120 km with several intense episodes lasting for a few minutes extending from 11:40 to 12:40 UT. The maximum heating rate reaches over 3 K/s at ~11:50 UT. This strong heating changes the pressure gradient and leads to a horizontal divergence of air flow above 120 km. The induced large upward vertical motion reaches ~80 m/s around 200 km at ~12:00 UT, with a time delay of ~10 min after Joule heating peaks (Figure 5b). Accompanying this upward motion and the resultant atmosphere expansion is the adiabatic cooling reaching a negative maximum of 0.6 K/s at ~200 km (Figure 5c), consistent with the altitude where the vertical upward motion is the strongest. Since temperature peaks around 150 km, such an upward motion also transports cold air upward below the peak, leading to cooling (up to 0.6 K/s) below 150 km. Above the peak, this upward motion brings warm air at 150 km upward, leading to heating (up to 0.3 K/s) at higher altitudes (Figure 5e). Horizontal heat advection and heat conduction tend to be moderate during most of the time and play minor roles below 250 km (Figures 5f and 5g). The time series of these heating/cooling terms at ~120 and ~200 km are shown in Figures 5d and 5h, respectively. Joule heating (red line) is dominant at ~120 km, while adiabatic cooling (blue line) becomes strong at ~200 km. Vertical advection (black line) induces cooling at ~120 km, while warming at ~200 km. The effects of horizontal heat advection + heat conduction (green line) are small at both altitudes compared to the other terms.

To further identify which heating/cooling terms play the dominant roles in shaping TTEIL, we perform a post processing diagnostic analysis of the temperature evolution induced by each individual term on the RHS of Equation 2 and by various combinations of these terms. For considering the impact of an individual term, we start from zero and add up the time integration of ∂T/∂t on fixed pressure levels only caused by this term in order to examine the net temperature changes. Figures 6a–6d show the temperature profiles by only integrating Joule heating, adiabatic cooling, vertical heat advection, horizontal heat advection, and heat conduction, respectively. For the different combination of these terms, we start from an initial temperature profile and perform similar temperature integrations (Figures 6e–6g). Since the intense Joule heating mainly occurs after 11:30 UT, after which neutral atmosphere starts to respond and change dramatically, we choose the temperature profile at 11:30 UT as an initial state. TTEIL is a time-integrated result of the thermodynamic balance of heating/cooling terms; thus, an integrated view is suitable for diagnosing their relative contribution to temperature changes.

Figure 6a shows Joule heating alone is capable of producing a strong inversion layer with temperature increases by over 2000 K within 40 min (from 11:50 to 12:30 UT) and peaks around 120 km. Along with the reduced temperature induced by adiabatic cooling peaking at ~180 km (Figure 6b), a sharp inversion layer with a peak around 120 km and temperature drop reaching over 1500 K above the peak forms after

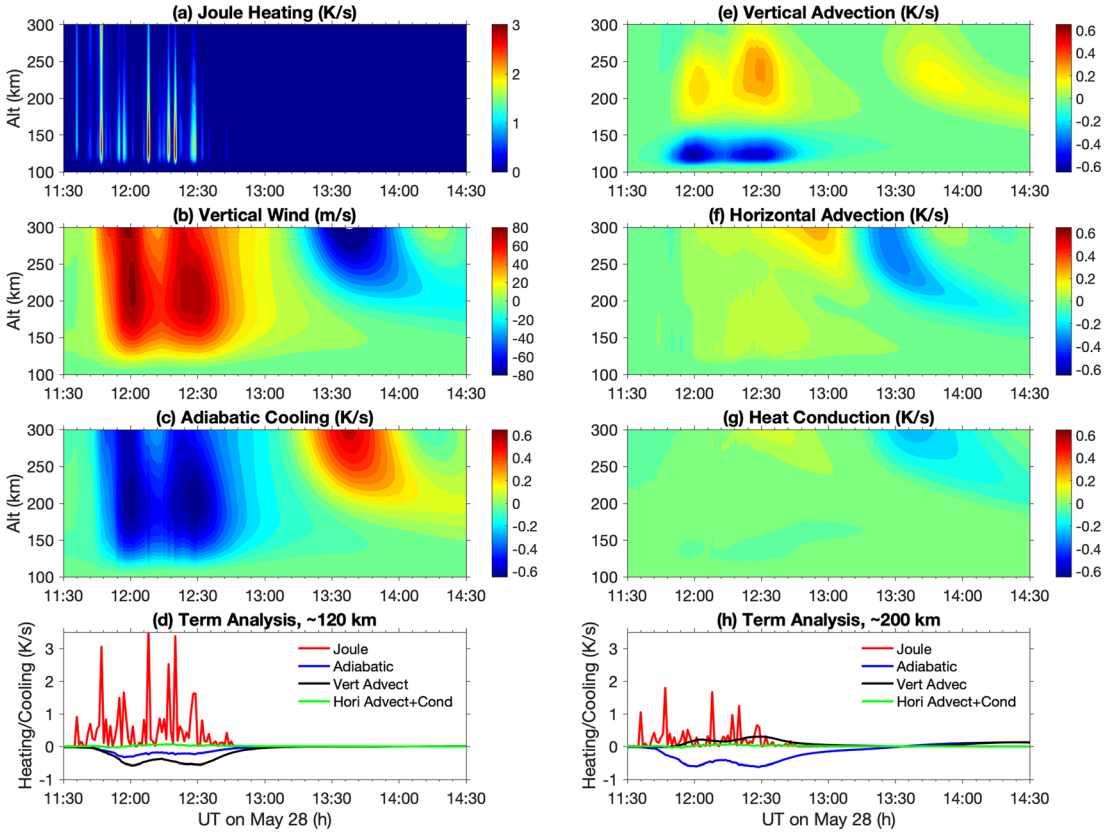

Figure 5. Temperature tendency (∂T/∂t) induced by (a) Joule heating, (c) adiabatic cooling, (e) vertical advection, (f) horizontal advection, and (g) heat conduction at (73.75°S, 117.5°W) where the maximum TTEIL is found. (b) Vertical winds at the same location. (d and h) ∂T/∂t induced by Joule heating, adiabatic cooling, vertical advection, and horizontal advection + conduction, at ~120 and ~200 km, respectively.

12:30 UT (Figure 6e). After accounting for the vertical heat advection (Figure 6c), however, the peak altitude where temperature reaches maximum moves up to ~150 km, and the inversion layer becomes much broader and weaker (Figures 6f, after 12:00 UT, and 6i). This indicates that vertical heat advection which cools the layer below 150 km and warms it above cancels out the sharp temperature gradient formed by Joule heating and adiabatic cooling in the lower thermosphere, thereby hinders the formation of a sharp TTEIL with the peak at a very low altitude. Horizontal advection and heat conduction play a minor role in shaping the temperature profile below 200 km by comparing Figures 6f and 6g, which is consistent with their small heating/cooling effects (Figures 5f, 5g, and 6d). By comparing Figures 6g and 6h, the overall temperature evolution is similar and the differences mainly originate from the numerical smoothing effect, which is not included in the thermodynamic equation (Shapiro, 1970) but implemented at every time step in the model to maintain numerical stability.

From Figures 5 and 6, the physical processes in generating the primary TTEIL in the model are summarized as follows: (1) strong Joule heating penetrating down to 120 km in a relative short period of time changes the pressure gradient and a horizontal divergence of air flow induces upward air motion; (2) upward wind induces strong adiabatic cooling reaching a maximum at ~200 km; (3) strong heating at ~120 km and cooling at ~200 km lead to strong vertical differential heating (Figures 5d and 5h) and a sharp TTEIL; and (4) vertical heat advection, on the other hand, acts as a strong cooling term below ~150 km and a moderate heating term above (Figure 5e), therefore playing a negative effect in forming the sharp TTEIL in general (Figure 6i). Therefore, the strong Joule heating is a trigger while the neutral dynamic terms including adiabatic cooling and vertical advection contribute to the formation and the ultimate structure of the TTEIL in the model simulation.

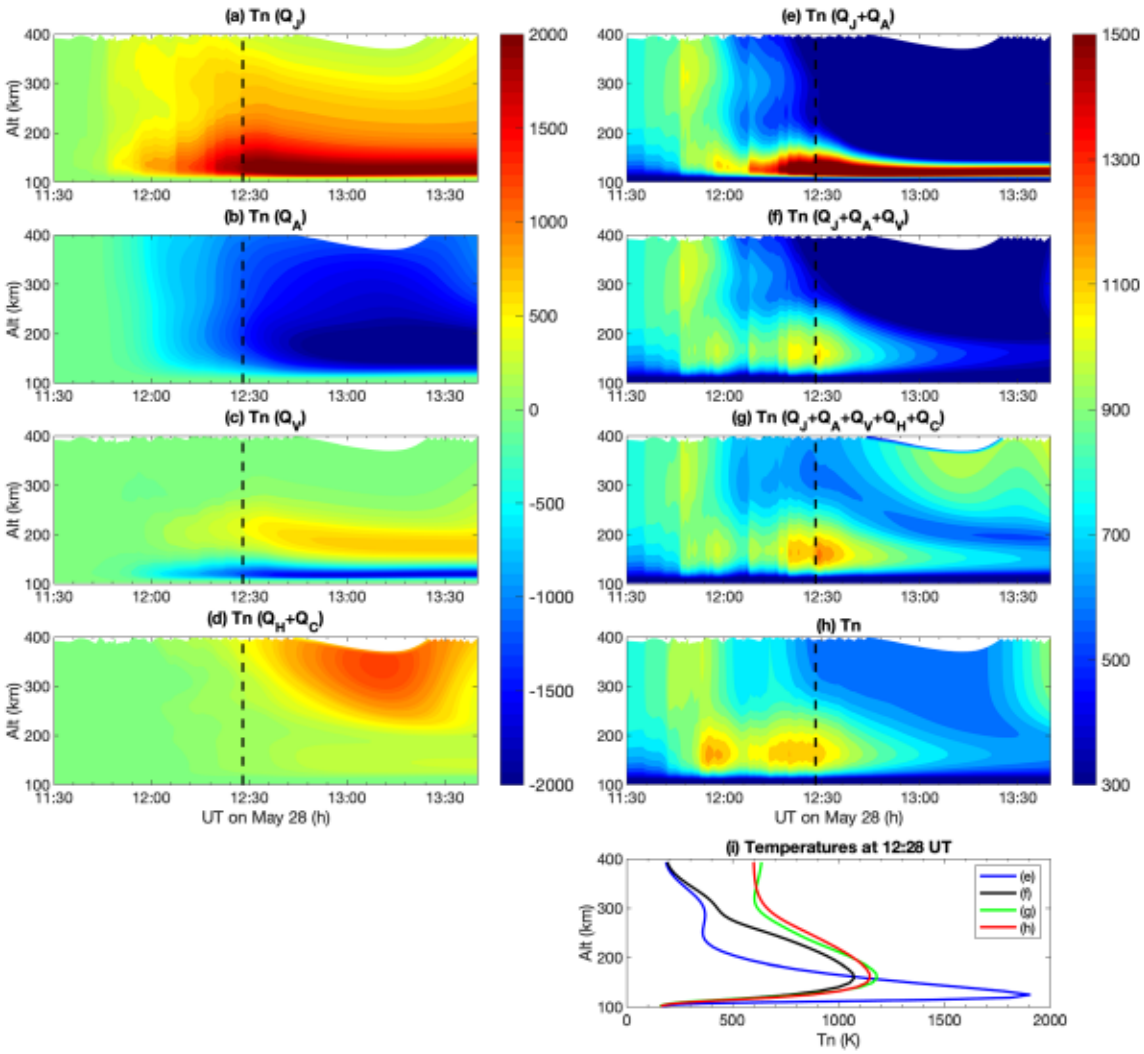

Figure 6. Temperature profiles at (73.75°S, 117.5°W) forced solely by (a) Joule heating (Q_J), (b) adiabatic cooling (Q_A), (c) vertical advection (Q_V), and (d) horizontal advection (Q_H) + heat conduction (Q_C), integrated from the initial state of zero temperatures at 11:30 UT. Temperature profiles forced by the combination of (e) $Q_J + Q_A$, (f) $Q_J + Q_A + Q_V$, and (g) $Q_J + Q_A + Q_V + Q_H + Q_C$. (h) The model results (Run 4) given as a reference. (i) The vertical temperature profiles of (e–h) at 12: 28 UT (dashed black lines in a–h), respectively. Units are K.

3.3. Electrodynamics and Neutral Dynamics Associated With Joule Heating

Joule heating $Q_J = \sigma_P (\mathbf{E} + \mathbf{u} \times \mathbf{B})^2$ is largely determined by Pedersen conductivity and electric fields. Figure 7 shows the time series of Pedersen conductivity, magnitude of total electric field $\left(\sqrt{E_x^2 + E_y^2}\right)$, and Joule heating interpolated to 150 km obtained from four different model runs. Considering that TTEIL is a large-scale phenomenon and the local electric fields are produced by adding random variabilities, the parameters shown in Figure 7 are averaged within the ambient nine grids around the location of primary TTEIL to form a regional and statistical picture. Comparing black and green lines with blue and red lines in Figure 7a, high-latitude conductivity calculated from the default E_m and Φ_E maps is elevated by ~3 times on average after incorporating the SSUSI auroral maps from 11:30 to 12:30 UT. The magnitudes of electric fields after adding variabilities demonstrate more variations with time than the original AMIE fields, while their means remain at a comparable level (Figure 7b). Such large electric field variations are also reported in the literature (e.g., Heppner, 1972); in real-time observations from Special Sensors-Ions, Electrons, and Scintillation (SSIES) onboard DMSP, large spikes in ion drifts are also identified which indicates large variations in electric fields (to be discussed in section 3.5). The combined effects of the enhanced conductivity

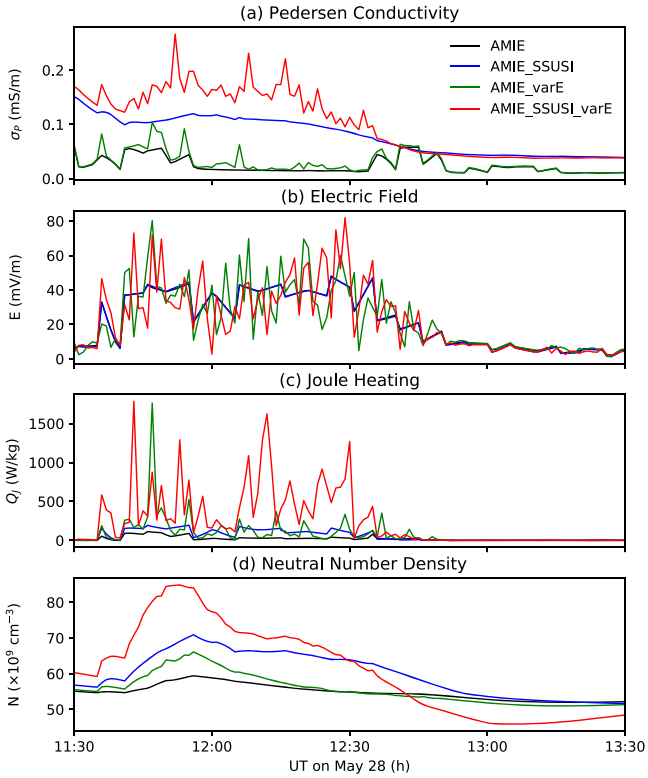

Figure 7. TIEGCM simulation of (a) Pedersen conductivity, (b) electric field magnitude, (c) Joule heating, and (d) neutral number density averaged within nearest 9 points around (73.75°S, 117.5°W) at 150 km. The model results from Runs 1 to 4 are indicated in black, blue, green, and red, respectively.

and electric field variability lead to a dramatic enhancement of Joule heating after 11:30 UT. The comparison of the green and blue lines with the red line in Figure 7c illustrates that increasing conductivity or adding electric field variability alone cannot enhance Joule heating significantly. Therefore, both realistic auroral precipitation and electric field (including its mean and variability), as the two critical high-latitude drivers of I-T models, are important for calculating Joule heating and the resultant neutral atmosphere responses (Zhu et al., 2020).

Using the same SSUSI-modified auroral maps, Figure 7a shows that Pederson conductivity from Run 4 (red) is larger than that from Run 2 (blue). Adding the electric field variability, which alters local Joule heating and then neutral temperature and number density (converted from neutral mass density using mean molar mass calculated from mass mixing ratios of O, O_2 and N_2), tends to impose a feedback on the local conductivity which is determined by both neutral and plasma densities (Kelley, 2009). Neutral number density shown in Figure 7d is higher in Run 4 than in Run 3 while plasma density barely changes at 150 km (not shown here), which suggests that neutral number density is mainly responsible for the conductivity change. The increase of local neutral number density in Run 4 is likely associated with the thermal expansion of the air below this altitude triggered by the enhanced Joule heating, and the denser air supplied from below leads to the increase of neutral number density at this altitude (150 km).

The global effect of Joule heating enhancement on neutral dynamics is also examined. Figure 8 shows the polar view of Joule heating, TTEIL magnitude (defined in section 3.1), neutral temperatures and vertical winds at two different altitudes in geographic coordinates. As shown in Figures 8(1a) and 8(1b), TTEIL emerges where Joule heating is intense (the maximum integrated Joule heating reaches ~1 W/m^2). Large vertical wind is present at both ~165 and ~222 km (Figures 8($1d_1$) and 8($1d_2$)) while neutral temperatures increase at lower altitudes but decreases at higher altitudes (Figures 8($1c_1$) and 8($1c_2$)) due to the strong differential heating. This picture is consistent with what are shown in Figures 5 and 6. An intriguing feature is the wave-like perturbations in temperatures and vertical winds, which propagate outward from the primary TTEIL region with time indicating a large-scale traveling atmospheric disturbance (TAD) structure. By perturbing the neutral dynamics in the surrounding environment, the TTEIL itself also propagates outward spirally and forms TTEIL at other locations as shown in Figure 8(2b). At ~12:53 UT, the front of the TTEIL approaches McMurdo (Figure 8(2b)), but with a magnitude significantly reduced (compared to Figure 8(1b)). The magnitude of TTEIL at McMurdo remains similar and then gradually diminishes afterward. The movie "polar_neutral.mp4" in the supporting information (SI) file provides a time-varying view of the above processes.

3.4. Comparison of Neutral Mass Densities With Satellite Observations

Figure 7d shows that the neutral number density increases at 150 km in Run 4 compared with the other runs. In order to examine whether the neutral mass density from our modified simulations is in a reasonable scope, we compare the neutral mass densities from the four different runs with the GRACE measurements in Figure 9a. All simulation results are projected along the satellite orbit and interpolated vertically to the satellite altitude (475 km). The corresponding GRACE orbit as a function of magnetic latitude, magnetic local time, geographic latitude, and solar local time is indicated in Figure 9b. The neutral mass density from the control run underestimates the GRACE observations by ~40% during the geomagnetically active period. This underestimation is consistent with the previous studies showing that the default configurations of I-T models tend to underestimate the neutral mass densities along satellite orbits during geomagnetically active times likely due to the underestimation of Joule heating (e.g., Deng et al., 2013; Shim et al., 2012). After

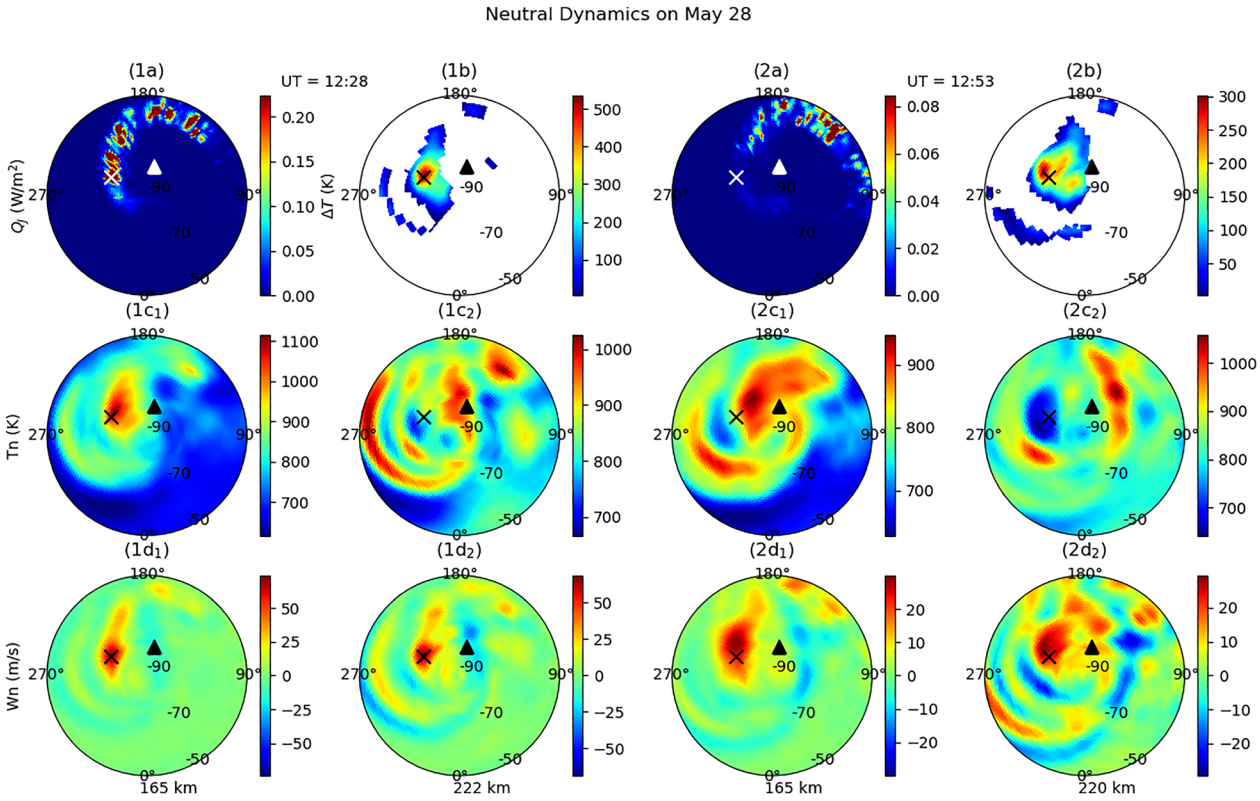

Figure 8. Spatial distribution of (1a) height integrated Joule heating, (1b) TTEIL magnitude, neutral temperatures at ($1c_1$) 165 and ($1c_2$) 222 km, and vertical winds at ($1d_1$) 165 and ($1d_2$) 222 km, at 12:28 UT in geographic coordinates. The 180° longitude is plotted at the top for a better visualization of the TTEIL propagation (see the movie provided in SI). The right two columns are the same except for 12:53 UT and the two examined altitudes are 165 and 220 km. Cross and triangle represent the location of the strongest TTEIL (73.75°S, 117.5°W) and McMurdo (77.8°S, 166.7°E), respectively.

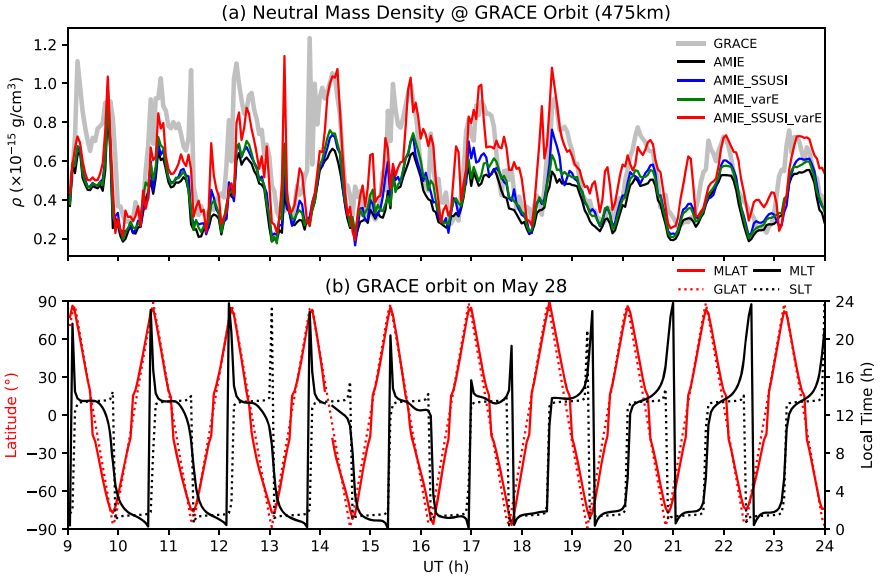

Figure 9. (a) Neutral mass densities projected along the GRACE orbit from the four different TIEGCM runs (colored lines) and the comparison with GRACE observations (gray line). (b) GRACE orbit during the time: Red solid line shows magnetic latitude, and black solid line shows magnetic local time; red dotted line shows geographic latitude, and black dotted line shows solar local time.

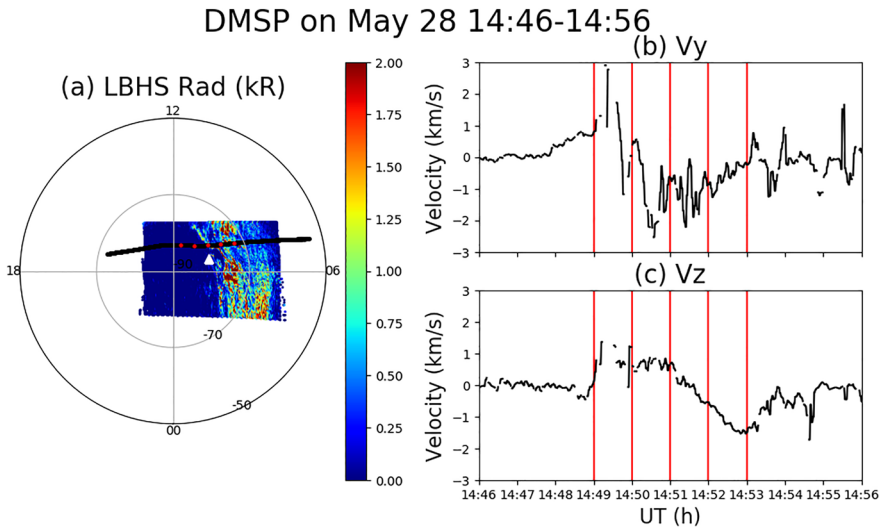

Figure 10. (a) DMSP F16 SSUSI observation of spectral radiance at LBHS band from 14:46 to 14:56 UT in magnetic latitude/local time coordinate; black line marks satellite orbit which travels from right to left; red dots mark the spatial locations of five consecutive time ticks; white triangle denotes McMurdo. (b and c) DMSP F16 SSIES measurements of cross-track ion drift (V_y) and vertical ion drift (V_z) from IDM during the same time period. Red vertical lines mark five consecutive time ticks in (a).

SSUSI auroral maps and electrical field variabilities are both implemented in the model, the simulated neutral mass density is overall elevated and best matches the observations (red and gray lines in Figure 9a). The better agreements with observations are found not only in high-latitude nightside regions where the modification of the model drivers is made but also in high-latitude dayside and low-latitude regions, which imply that the neutral densities around 475 km can be affected by neutral dynamics (such as TADs) induced by remote heating sources. Overall, the model-GRACE comparison suggests that our modification in both aurora and electric field which increases Joule heating generally improves the simulation of neutral mass density response to the storm globally.

A closer examination on Figure 9 shows at some locations (e.g., time around 9.5, 11, 14, and 15.5 UT), model simulations are still smaller than observations. Some of the underestimations occur in dayside high-latitude regions (such as 14 and 15.5 UT), which might be related to localized field-aligned currents (FACs) in the cusp region (Lühr et al., 2004). Since the current TIEGCM runs do not treat FACs in the cusp region as an explicit input, the reasons for the discrepancy deserve more detailed investigation in future studies. The underestimations in nighttime high-latitude regions such as those around 13 and 14.5 UT may be more directly related to Joule heating being still underestimated locally. This is not unexpected since the interpolation and binning method for auroral maps and AMIE may miss the localized real-time auroral precipitation and electric field, respectively. For instance, at any specific point, such as McMurdo, the satellite (SSUSI) observations cover a very small portion of the time series, so most of the auroral precipitation at a particular location used in TIEGCM have to be interpreted from the scarce observations plus the empirical model (section 2.2). In addition, electric field variability in the model is added as a random number, which may also miss the realistic features locally.

3.5. TTEIL Structure at McMurdo With Local Joule Heating Enhancement

Indeed, the underestimation of electric field fluctuation is seen at McMurdo. During the time window of 14:46–14:56 UT when the TTEIL was detected by lidar (~15 UT), DMSP F16 has conjunction measurements (Figure 10a). Satellite orbit is marked as black line which goes from right to left. Strong spectral radiances in Lyman-Birge-Hopfield short (LBHS) band observed by SSUSI appear very close to McMurdo at ~14:50 UT (Figure 10a). During the same time window, ion drift measurements from ion drift meter (IDM) in SSIES on DMSP show large spikes (up to 3 km/s) and fluctuations indicating strong local electric field near McMurdo (Figures 10b and 10c). Red vertical lines mark five consecutive time ticks with the corresponding orbit locations marked as red dots in Figure 10a. The large ion drift (3 km/s) is identified within auroral

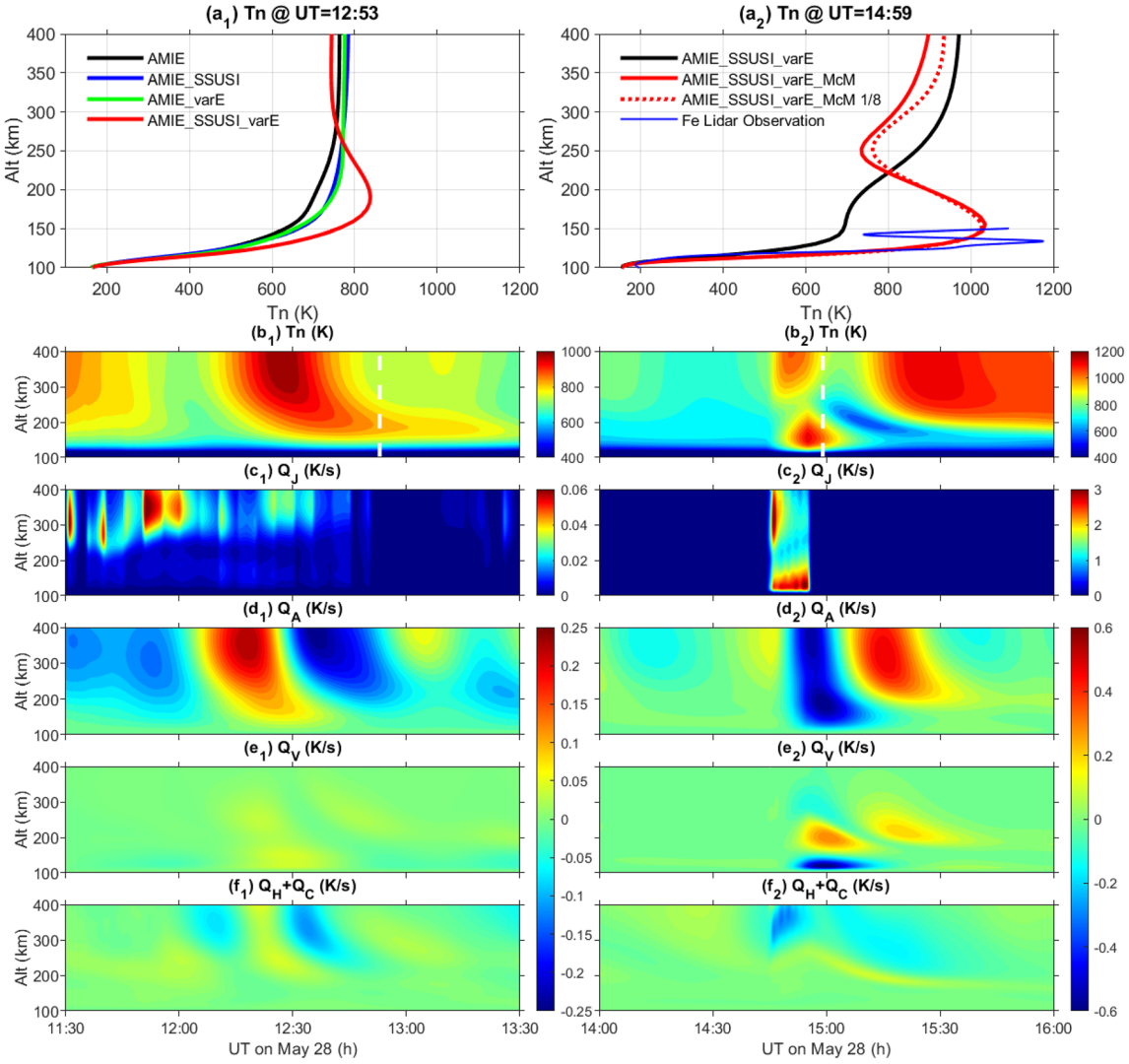

Figure 11. (a_1) Vertical temperature profiles from Runs 1 to 4 at 12:53 UT, McMurdo. (a_2) Vertical temperature profiles from Runs 4 and 5 at 14:59 UT, McMurdo; the temperature profile from high-resolution configuration of Run 5 (AMIE_SSUSI_varE_McM 1/8) at 14:55 UT are also plotted in red dashed line. (b_1–f_1) Temporal variations of neutral temperature, Joule heating, adiabatic heating/cooling, vertical advection, and horizontal advection + heat conduction at McMurdo, obtained from Run 4. (b_2–f_2) Same as (b_1)–(f_1) except that the results are obtained from Run 5 during a different time period.

region. Such auroral enhancement and rapid-varying large electric field near McMurdo are not captured in Run 4. Therefore, after the TTEIL signal propagates to McMurdo at 12:53 UT in Run 4 with rather a small magnitude (Figure 11a_1, red line), it does not last for long and the TTEIL structure is missing at ~15 UT (Figure 11a_2, black line). The discrepancies both in timing and TTEIL magnitude at McMurdo prompt us to further consider the localized high-latitude drivers by incorporating DMSP observations around McMurdo and examining the temperature responses.

Run 5 (named AMIE_SSUSI_varE_McM) is performed based on the settings of Run 4 but with enhanced auroral precipitation and electric field added around McMurdo. We set auroral mean energy to be 10 keV and energy flux to be 30 erg/cm^2/s from 14:45 to 14:55 UT, during which McMurdo is located at the poleward edge of the aurora oval (Figure 10a). Within this time period, we impose an electric field of 150 mV/m in the north/south direction (E_y) with flipping direction every 2 min similar to Deng et al. (2009) and Zhu et al. (2018). Note that the evolution of DMSP ion drifts shown in Figures 10b and 10c contains both temporal and spatial variations. They provide a reference for the possible magnitudes but not exact values of the electric fields over McMurdo. The direction and magnitude of electric fields are chosen to reproduce

ion drifts with magnitude comparable to the maximum IDM observation (Figure 10b), in which the cross-track ion drifts are largely oriented along eastward/westward direction. Auroral energy and electric field are both tuned in order to reproduce a similar magnitude of temperature peak close to the lidar observation. Such local adjustment is implemented uniformly in a region centered at (78.75°S, 167.5°E) with a spatial expansion of three grid points in latitude and seven grids in longitude. Imposing additional electric field in the east/west direction (E_x) is also done but the difference between these two tests are small, thus not shown here.

The simulation results are shown in Figures $11a_2$–$11f_2$. Compared with the results from Run 4 at the same location and time (black line in Figure $11a_2$), the temperature inversion structure in Run 5 (red line) is more prominent and the temperature peak is larger and closer to the lidar observation (over 1000 K). This temperature structure is also comparable with the primary TTEIL studied in section 3.2. The heating term analysis shows that Joule heating is the strongest thermal term and it penetrates down to ~120 km. The second and third dominant terms are the resulting strong adiabatic cooling accompanying the upward motion and vertical advection. Again, similar to the mechanism for the primary TTEIL formation studied in section 3.2, Joule heating leads to temperature increase below ~150 km, adiabatic cooling leads to temperature decrease above ~120 km altitude, and along with vertical advection, these three terms determine the vertical structure of neutral temperature.

To show the unique features associated with the primary TTEIL generated at McMurdo in Run 5, the same term analysis is carried out for the weak TTEIL identified around 12:53 UT in Run 4 for comparison (Figure $11b_1$-f_1). In Run 5, the strong Joule heating penetrates all the way down to ~120 km and produces a secondary and also stronger peak in the E region than the F region peak around 300 km (Figure $11c_2$). In Run 4, the F region peak is more prominent and the penetration to the E region is insignificant (Figure $11c_1$). Distinct from Run 5, adiabatic heating/cooling is the strongest thermal term in Run 4, which also contributes the most to the morphology of the weak TTEIL according to the analysis of integrated temperature profiles (not shown here). The alternating adiabatic heating/cooling is likely induced by the vertical wind perturbation due to the propagation of TADs. The comparison between Runs 4 and 5 indicates that for the TTEIL formation at different times/locations, the relative importance of Joule heating, adiabatic cooling, vertical advection, horizontal advection, and heat conduction can change. For the formation of primary TTEIL (characterized by extremely large temperature enhancement and large TTEIL magnitude), the localized strong Joule heating is a critical trigger, which likely happened at McMurdo. For the weak TTEIL, the dynamics associated with wave-induced transport and disturbances may play dominant roles.

4. Discussion

Through the refinement of the high-latitude drivers in a global sense and further fine tuning their localized characteristics around McMurdo, Run 5 captures a more realistic temperature elevation at McMurdo and compares better with the lidar observations in neutral temperature than the other runs. Despite numerous improvements, there are still noticeable discrepancies between the model simulation and lidar observations by comparing Figure $11a_2$ and Figure 1a. The peak altitude is about 20 km higher than the observation (~130 km), and the modeled layer width is much broader than the observation. To sort out possible causes for the discrepancies, we have performed a few other tests even though they turn out to be insufficient to resolve these issues. To give a reference for future modeling, we list them as follows:

1. Test of the model lower boundary: The same modifications of high-latitude drivers are implemented into TIMEGCM (Roble & Ridley, 1994), which is governed by similar dynamic and thermodynamic equations in the upper atmosphere as the TIEGCM but with a lower boundary at ~30 km. The simulated TTEIL still has the same peak altitude at ~150 km, which suggests that the lower boundary of TIEGCM (~97 km) close to the observed TTEIL is likely not the main reason for the high peak altitude in the simulations.
2. To examine whether the broad vertical span is due to the "strong" diffusion coefficients, we decrease the eddy diffusion coefficient (K_E) and heat conduction coefficient (K_T) in the model to half. The test results show that the vertical temperature structure does not differ much from what is shown in Figure 4, which is consistent with the minor contribution from the diffusion terms in the thermodynamic term analysis (section 3.2).

3. The possibility of high altitude for temperature peak and broad span due to low vertical resolution is also examined by performing the high-resolution (1.25° in latitude and longitude, 1/8 scale height) TIEGCM run. The vertical temperature profiles from high-resolution model run using the settings for Run 5 (named AMIE_SSUSI_varE_McM 1/8) is illustrated as the red dashed line in Figure 11a$_2$. Intensifying aurora and electric field around McMurdo produce nearly the same temperatures as the normal resolution run below 220 km but the maximum magnitude of TTEIL occurs 4 min earlier. The altitude for the peak temperature enhancement (~150 km) and the mechanism for producing the TTEIL at McMurdo are the same.
4. Liu et al. (2016) found that the electron temperature can increase by ~2000 K at 100–130 km due to Farley-Buneman instability (FBI), but it is not known whether such instability can also lead to a significant neutral temperature increase. We test this possibility by implementing the electron anomalous heating module resulting from the FBI and find that neutral temperature is only elevated by several Kelvin. Such an insignificant neutral temperature change may be caused by the fact that the electron to neutral density ratio at this altitude is so small that the energy exchange from electrons to neutrals is not sufficient to heat the neutrals, leaving neutral temperatures almost unchanged.

It should be noted that the above test results and their implication rely on physics, chemistry, and electrodynamics considered in TIEGCM. The effects from the processes that are not considered in the model such as nonhydrostatic processes, local heating induced by wave breaking cannot be tested for now. In addition, gravity wave activities in the lower boundary of TIEGCM have not been included at a level comparable to observations (Chen et al., 2016; Chu et al., 2011), so their effects are not considered in the current model. The narrow width of the observed TTEIL, likely associated with a vertically propagating wave structure (Figure 1a), could be a combined effect from the wave perturbations in electrodynamic or neutral dynamic processes (Chu & Yu, 2017) superimposed on the elevated temperature background. Testing all these possibilities is out of the scope of this study and deserves further investigation.

5. Conclusions

To understand the underlying physics for the large thermospheric temperature enhancement (~550 K at ~130 km) and inversion layer (TTEIL) structure observed by lidar at McMurdo during a geomagnetic storm on 28 May 2011, we modify auroral maps and electric field variabilities in the TIEGCM with guidance from the DMSP observations and previous statistical results from SuperDARN. Such modifications are made because the default model runs with empirical high-latitude drivers cannot adequately reproduce storm responses. We first incorporate auroral precipitation observed by DMSP/SSUSI into the auroral maps, which lead to increased conductivity. On average, Pedersen conductivity increases by 3 times at ~150 km in the auroral region during the active period. We then take the subgrid scale electric field variabilities into account by adding a randomly generated number in the auroral region to the original electric field obtained from AMIE. Two steps of modifications are implemented to cover high-latitude regions first and then focus on the local region around McMurdo. The modifications bring the simulation of neutral densities close to the GRACE observations and generate the TTEIL sharing similarities with lidar observations.

The most important effects of the modified auroral precipitation and electric field variability are large enhancements in Joule heating and its deeper penetration. To generate the primary TTEIL including the one observed at McMurdo, the local intense Joule heating is an important factor that not only provides the heating source down to ~120 km but also triggers the following dynamical processes that work together with Joule heating to shape the ultimate temperature structure. Associated with the intense Joule heating, pressure gradient changes and large upward winds of over 80 m/s resulting from a horizontal divergence of air flow lead to strong adiabatic cooling at high altitudes (0.6 K/s maximizing at ~200 km). Strong Joule heating at ~120 km and adiabatic cooling higher up result in strong differential heating vertically and generate a sharp temperature inversion. In the contrary, vertical heat advection induces strong cooling (0.6 K/s) below 150 km and moderate heating above (0.3 K/s) mainly due to the upward vertical motion and the temperature peak at ~150 km. Therefore, vertical advection weakens the TTEIL and renders a higher temperature peak altitude and a broader layer than the observations. The vertical structure of the primary TTEIL is mainly determined by the combined effects of these three thermodynamic terms. Simulation results also show that TADs are generated from where the maximum Joule heating is deposited and the

primary TTEIL is generated. The TADs propagate outward to other locations, forming TTEILs with much smaller magnitudes than the primary ones in distant regions. For the weak TTEIL, the local Joule heating is minimal and temperature structure can be mainly determined by other terms such as adiabatic heating/cooling effects.

The improved agreement with the observed neutral density and temperature in our modified simulations indicates the importance of regional-scale auroral precipitation and electric fields as two critical high-latitude drivers in the I-T models. Our results also imply that the local fine-scale characteristics of high-latitude drivers, which are often missing in empirical drivers are nevertheless essential for the simulation of local storm-time dynamics. Run 5, which incorporates the high-latitude modification of auroral maps and electric field variability, along with additional local enhancement in Joule heating around McMurdo, reasonably reproduces the dramatic temperature enhancement in the lower thermosphere observed by the lidar, but the modeled peak altitude is still higher (~150 km) than the observed one (~130 km). Note that the amount of heating needed in the modeling is large (maximum value is on the order of 1 W/m^2), but it is not implausible. We suspect that this much heating may require, in reality, some physics not included in the current TIEGCM, for example, strong anomalous heating associated with plasma irregularities, in addition to the missing physics mentioned earlier. The unsolved discrepancies and the possible modeling efforts to tackle this problem remain as open questions.

Data Availability Statement

Other data sources of this paper are omniweb.gsfc.nasa.gov (geomagnetic indices), ground magnetometer data are obtained from supermag.jhuapl.edu (SuperMAG), satellite magnetometer data are obtained from ampere.jhuapl.edu (AMPERE), ion drift data are obtained from vt.superdarn.org (SuperDARN), particle precipitation data are obtained from cedar.openmadrigal.org (DMSP/SSJ), and auroral imager data are obtained from ssusi.jhuapl.edu (DMSP/SSUSI). The data in this work can be downloaded from data.mendeley.com/datasets/7sv5nt5j5k/2.

Acknowledgments

We are grateful for Arthur D. Richmond for his critical internal review and suggestions. We thank Marc Hairston for providing the DMSP SSIES data, Shuanggen Jin for providing the GRACE data, and Jing Liu for providing the electron anomalous heating module. The high-resolution version of TIEGCM is developed with the assistance of Tong Dang. We acknowledge Timothy Fuller-Rowell, Ryan McGranaghan, Zhonghua Xu, Xu Zhou, and Qingyu Zhu for their invaluable comments and suggestions. We appreciate the technical support from Clemson Computing and Information Technology (CCIT) team. X. L. and H. W.'s work was partially supported by NASA NNX17AG10G and NSF grants AGS-1705448, OPP-1705450, and CAREER-1753214. G. L. was supported by the Living with a Star program under NASA grant 80NSSC17K071 and the Heliophysics Supporting Research program under NASA grant NNX17AI39G. X. C. was partially supported by NSF grants OPP-1246405, OPP-1443726, and AGS-1452351. W. W. was partially supported by the NASA Heliophysics Supporting Research program under NASA grants NNX17I42G and 80NSSC19K0835. D. K. and L. K. were partially supported by AFOSR award FA9550-17-1-0258 and AFOSR MURI award FA9550-16-1-0364.

References

Anderson, B. J., Korth, H., Waters, C. L., Barnes, R. M., & Weiss, M. B. (2008). The Active Magnetosphere and Planetary Electrodynamics Response Experiment (AMPERE): A new facility for real-time magnetosphere-ionosphere monitoring, American Geophysical Union Fall Meeting Abstracts, SA51A–1550

Anderson, B. J., Korth, H., Waters, C. L., Green, D. L., Merkin, V. G., Barnes, R. J., & Dyrud, L. P. (2014). Development of large-scale Birkeland currents determined from the active magnetosphere and planetary electrodynamics response experiment. *Geophysical Research Letters*, *41*, 3017–3025. https://doi.org/10.1002/2014GL059941

Chen, C., Chu, X., Zhao, J., Roberts, B. R., Yu, Z., Fong, W., et al. (2016). Lidar observations of persistent gravity waves with periods of 3–10 h in the Antarctic middle and upper atmosphere at McMurdo (77.83°S, 166.67°E). *Journal of Geophysical Research: Space Physics*, *121*, 1483–1502. https://doi.org/10.1002/2015JA022127

Chi, Y., Zhang, J., Shen, C., Hess, P., Liu, L., Mishra, W., & Wang, Y. (2018). Observational study of an Earth-affecting problematic ICME from STEREO. *The Astrophysical Journal*, *863*(1), 108. https://doi.org/10.3847/1538-4357/aacf44

Chisham, G., Lester, M., Milan, S. E., Freeman, M. P., Bristow, W. A., Grocott, A., et al. (2007). *Surveys in Geophysics*, *28*(1), 33–109. https://doi.org/10.1007/s10712-007-9017-8

Chu, X., Pan, W., Papen, G. C., Gardner, C. S., & Gelbwachs, J. A. (2002). Fe Boltzmann temperature lidar: Design, error analysis, and initial results at the North And South Poles. *Applied Optics*, *41*(21), 4400–4410. https://doi.org/10.1364/AO.41.004400

Chu, X., & Yu, Z. (2017). Formation mechanisms of neutral Fe layers in the thermosphere at Antarctica studied with a thermosphere-ionosphere Fe/Fe+ (TIFe) model. *Journal of Geophysical Research: Space Physics*, *122*, 6812–6848. https://doi.org/10.1002/2016JA023773

Chu, X., Yu, Z., Gardner, C. S., Chen, C., & Fong, W. (2011). Lidar observations of neutral Fe layers and fast gravity waves in the thermosphere (110–155 km) at McMurdo (77.8°S, 166.7°E), Antarctica. *Geophysical Research Letters*, *38*, L23807. https://doi.org/10.1029/2011GL050016

Codrescu, M. V., Fuller-Rowell, T. J., & Foster, J. C. (1995). On the importance of *E*-field variability for Joule heating in the high-latitude thermosphere. *Geophysical Research Letters*, *22*(17), 2393–2396. https://doi.org/10.1029/95GL01909

Codrescu, M. V., Fuller-Rowell, T. J., Foster, J. C., Holt, J. M., & Cariglia, S. J. (2000). Electric field variability associated with the Millstone Hill electric field model. *Journal of Geophysical Research*, *105*(A3), 5265–5273. https://doi.org/10.1029/1999JA900463

Codrescu, M. V., Fuller-Rowell, T. J., Munteanu, V., Minter, C. F., & Millward, G. H. (2008). Validation of the coupled thermosphere ionosphere plasmasphere electrodynamics model: CTIPE-Mass Spectrometer Incoherent Scatter temperature comparison. *Space Weather*, *6*, S09005. https://doi.org/10.1029/2007SW000364

Cole, K. D. (1975). Energy deposition in the thermosphere caused by the solar wind. *Journal of Atmospheric and Terrestrial Physics*, *37*(6–7), 939–949. https://doi.org/10.1016/0021-9169(75)90008-2

Cosgrove, R., McCready, M., Tsunoda, R., & Stromme, A. (2011). The bias on the Joule heating estimate: Small-scale variability versus resolved-scale model uncertainty and the correlation of electric field and conductance. *Journal of Geophysical Research*, *116*, A09320. https://doi.org/10.1029/2011JA016665

Cosgrove, R. B., & Codrescu, M. (2009). Electric field variability and model uncertainty: A classification of source terms in estimating the squared electric field from an electric field model. *Journal of Geophysical Research*, *114*, A06301. https://doi.org/10.1029/2008JA013929

Cosgrove, R. B., Lu, G., Bahcivan, H., Matsuo, T., Heinselman, C. J., & McCready, M. A. (2009). Comparison of AMIE-modeled and Sondrestrom-measured Joule heating: A study in model resolution and electric field-conductivity correlation. *Journal of Geophysical Research*, *114*, A04316. https://doi.org/10.1029/2008JA013508

Cousins, E. D. P., & Shepherd, S. G. (2012a). Statistical characteristics of small-scale spatial and temporal electric field variability in the high-latitude ionosphere. *Journal of Geophysical Research*, *117*, A03317. https://doi.org/10.1029/2011JA017383

Cousins, E. D. P., & Shepherd, S. G. (2012b). Statistical maps of small-scale electric field variability in the high-latitude ionosphere. *Journal of Geophysical Research*, *117*, A12304. https://doi.org/10.1029/2012JA017929

Deng, Y., Fuller-Rowell, T. J., Ridley, A. J., Knipp, D., & Lopez, R. E. (2013). Theoretical study: Influence of different energy sources on the cusp neutral density enhancement. *Journal of Geophysical Research: Space Physics*, *118*, 2340–2349. https://doi.org/10.1002/jgra.50197

Deng, Y., Huang, Y., Lei, J., Ridley, A. J., Lopez, R., & Thayer, J. (2011). Energy input into the upper atmosphere associated with high-speed solar wind streams in 2005. *Journal of Geophysical Research*, *116*, A05303. https://doi.org/10.1029/2010JA016201

Deng, Y., Maute, A., Richmond, A. D., & Roble, R. G. (2009). Impact of electric field variability on Joule heating and thermospheric temperature and density. *Geophysical Research Letters*, *36*, L08105. https://doi.org/10.1029/2008GL036916

Emery, B. A., Lathuillere, C., Richards, P. G., Roble, R. G., Buonsanto, M. J., Knipp, D. J., et al. (1999). Time dependent thermospheric neutral response to the 2–11 November 1993 storm period. *Journal of Atmospheric and Solar-Terrestrial Physics*, *61*(3–4), 329–350. https://doi.org/10.1016/S1364-6826(98)00137-0

Fagundes, P. R., Sahai, Y., Takahashi, H., Gobbi, D., & Bittencourt, J. A. (1996). Thermospheric and mesospheric temperatures during geomagnetic storms at 23°S. *Journal of Atmospheric and Terrestrial Physics*, *58*(16), 1963–1972. https://doi.org/10.1016/0021-9169(96)00001-3

Forbes, J. M., Lu, G., Bruinsma, S., Nerem, S., & Zhang, X. (2005). Thermosphere density variations due to the 15–24 April 2002 solar events from CHAMP/STAR accelerometer. *Journal of Geophysical Research*, *110*, A12S27. https://doi.org/10.1029/2004JA010856

Fuller-Rowell, T. J., Rees, D., Quegan, S., Moffett, R. J., & Bailey, G. J. (1987). Interactions between neutral thermospheric composition and the polar ionosphere using a coupled ionosphere-thermosphere model. *Journal of Geophysical Research*, *92*(A7), 7744. https://doi.org/10.1029/JA092iA07p07744

Gjerloev, J. W. (2009). A global ground-based magnetometer initiative. *Eos, Transactions American Geophysical Union*, *90*(27), 230. https://doi.org/10.1029/2009EO270002

Gjerloev, J. W. (2012). The SuperMAG data processing technique. *Journal of Geophysical Research*, *117*, A09213. https://doi.org/10.1029/2012JA017683

Golovchanskaya, I. V., Ostapenko, A. A., & Kozelov, B. V. (2006). Relationship between the high-latitude electric and magnetic turbulence and the Birkeland field-aligned currents. *Journal of Geophysical Research*, *111*, A12301. https://doi.org/10.1029/2006JA011835

Greenwald, R. A., Baker, K. B., Dudeney, J. R., Pinnock, M., Jones, T. B., Thomas, E. C., et al. (1995). DARN/SuperDARN: A global view of the dynamics of high-latitude convection. *Space Science Reviews*, *71*(1–4), 761–796. https://doi.org/10.1007/BF00751350

Hardy, D. A., Gussenhoven, M. S., & Holeman, E. (1985). A statistical model of auroral electron precipitation. *Journal of Geophysical Research*, *90*(A5), 4229. https://doi.org/10.1029/JA090iA05p04229

Heelis, R. A., Lowell, J. K., & Spiro, R. W. (1982). A model of the high-latitude ionospheric convection pattern. *Journal of Geophysical Research*, *87*(A8), 6339. https://doi.org/10.1029/JA087iA08p06339

Heppner, J. P. (1972). Electric field variations during substorms: OGO-6 measurements. *Planetary and Space Science*, *20*(9), 1475–1498. https://doi.org/10.1016/0032-0633(72)90052-9

Heppner, J. P., Liebrecht, M. C., Maynard, N. C., & Pfaff, R. F. (1993). High-latitude distributions of plasma waves and spatial irregularities from DE 2 alternating current electric field observations. *Journal of Geophysical Research*, *98*(A2), 1629–1652. https://doi.org/10.1029/92JA01836

Huang, C. Y., & Burke, W. J. (2004). Transient sheets of field-aligned current observed by DMSP during the main phase of a magnetic superstorm. *Journal of Geophysical Research*, *109*, A06303. https://doi.org/10.1029/2003JA010067

Huang, Y., Wu, Q., Huang, C. Y., & Su, Y.-J. (2016). Thermosphere variation at different altitudes over the northern polar cap during magnetic storms. *Journal of Atmospheric and Solar-Terrestrial Physics*, *146*, 140–148. https://doi.org/10.1016/j.jastp.2016.06.003

Kadinsky-Cade, K., Holeman, E., McGarity, J., Rich, F., Denig, W., Burke, W., & Hardy, D. (2004). First results from the SSJ5 precipitating particle sensor on DMSP F16: simultaneous observation of keV and meV particles during the 2003 Halloween Storms, American Geophysical Union Spring Meeting Abstracts, SH53A-03

Kelley, M. C. (2009). *The Earth's Ionosphere: Plasma Physics and Electrodynamics* (Vol. 96). Cambridge, MA: Academic Press, Elsevier. https://doi.org/10.1016/S0074-6142(09)60212-6

Knipp, D., Eriksson, S., Kilcommons, L., Crowley, G., Lei, J., Hairston, M., & Drake, K. (2011). Extreme Poynting flux in the dayside thermosphere: Examples and statistics. *Geophysical Research Letters*, *38*, L16102. https://doi.org/10.1029/2011GL048302

Knipp, D. J., Emery, B. A., Richmond, A. D., Crooker, N. U., Hairston, M. R., Cumnock, J. A., et al. (1993). Ionospheric convection response to slow, strong variations in a northward interplanetary magnetic field: A case study for January 14, 1988. *Journal of Geophysical Research*, *98*(A11), 19,273–19,292. https://doi.org/10.1029/93JA01010

Knipp, D. J., Pette, D. V., Kilcommons, L. M., Isaacs, T. L., Cruz, A. A., Mlynczak, M. G., et al. (2017). Thermospheric nitric oxide response to shock-led storms. *Space Weather*, *15*, 325–342. https://doi.org/10.1002/2016SW001567

Knipp, D. J., Tobiska, W. K., & Emery, B. A. (2004). Direct and indirect thermospheric heating sources for solar cycles 21–23. *Solar Physics*, *224*(1–2), 495–505. https://doi.org/10.1007/s11207-005-6393-4

Laštovička, J. (1996). Effects of geomagnetic storms in the lower ionosphere, middle atmosphere and troposphere. *Journal of Atmospheric and Terrestrial Physics*, *58*(7), 831–843. https://doi.org/10.1016/0021-9169(95)00106-9

Lei, J., Thayer, J. P., Burns, A. G., Lu, G., & Deng, Y. (2010). Wind and temperature effects on thermosphere mass density response to the November 2004 geomagnetic storm. *Journal of Geophysical Research*, *115*, A05305. https://doi.org/10.1029/2009JA014754

Lei, J., Thayer, J. P., Lu, G., Burns, A. G., Wang, W., Sutton, E. K., & Emery, B. A. (2011). Rapid recovery of thermosphere density during the October 2003 geomagnetic storms. *Journal of Geophysical Research*, *116*, A03306. https://doi.org/10.1029/2010JA016164

Li, J., Wang, W., Lu, J., Yuan, T., Yue, J., Liu, X., et al. (2018). On the responses of mesosphere and lower thermosphere temperatures to geomagnetic storms at low and middle latitudes. *Geophysical Research Letters*, *45*, 10,128–10,137. https://doi.org/10.1029/2018GL078968

Li, J., Wang, W., Lu, J., Yue, J., Burns, A. G., Yuan, T., et al. (2019). A modeling study of the responses of mesosphere and lower thermosphere winds to geomagnetic storms at middle latitudes. *Journal of Geophysical Research: Space Physics*, *124*, 3666–3680. https://doi.org/10.1029/2019JA026533

Li, Z., Knipp, D., & Wang, W. (2019). Understanding the behaviors of thermospheric nitric oxide cooling during the 15 May 2005 geomagnetic storm. *Journal of Geophysical Research: Space Physics*, *124*, 2113–2126. https://doi.org/10.1029/2018JA026247

Liu, J., Wang, W., Oppenheim, M., Dimant, Y., Wiltberger, M., & Merkin, S. (2016). Anomalous electron heating effects on the E region ionosphere in TIEGCM. *Geophysical Research Letters*, *43*, 2351–2358. https://doi.org/10.1002/2016GL068010

Liu, X., Yue, J., Wang, W., Xu, J., Zhang, Y., Li, J., et al. (2018). Responses of lower thermospheric temperature to the 2013 St. Patrick's Day geomagnetic storm. *Geophysical Research Letters*, *45*, 4656–4664. https://doi.org/10.1029/2018GL078039

Lu, G., Baker, D. N., McPherron, R. L., Farrugia, C. J., Lummerzheim, D., Ruohoniemi, J. M., et al. (1998). Global energy deposition during the January 1997 magnetic cloud event. *Journal of Geophysical Research*, *103*(A6), 11,685–11,694. https://doi.org/10.1029/98JA00897

Lu, G., Goncharenko, L. P., Richmond, A. D., Roble, R. G., & Aponte, N. (2008). A dayside ionospheric positive storm phase driven by neutral winds. *Journal of Geophysical Research*, *113*, A08304. https://doi.org/10.1029/2007JA012895

Lu, G., Mlynczak, M. G., Hunt, L. A., Woods, T. N., & Roble, R. G. (2010). On the relationship of Joule heating and nitric oxide radiative cooling in the thermosphere. *Journal of Geophysical Research*, *115*, A05306. https://doi.org/10.1029/2009JA014662

Lu, G., Pi, X., Richmond, A. D., & Roble, R. G. (1998). Variations of total electron content during geomagnetic disturbances: A model/observation comparison. *Geophysical Research Letters*, *25*(3), 253–256. https://doi.org/10.1029/97GL03778

Lu, G., Richmond, A. D., Emery, B. A., & Roble, R. G. (1995). Magnetosphere-ionosphere-thermosphere coupling: Effect of neutral winds on energy transfer and field-aligned current. *Geophysical Research Letters*, *100*(A10), 19643. https://doi.org/10.1029/95JA00766

Lühr, H., Rother, M., Köhler, W., Ritter, P., & Grunwaldt, L. (2004). Thermospheric up-welling in the cusp region: Evidence from CHAMP observations. *Geophysical Research Letters*, *31*, L06805. https://doi.org/10.1029/2003GL019314

Matsuo, T., & Richmond, A. D. (2008). Effects of high-latitude ionospheric electric field variability on global thermospheric Joule heating and mechanical energy transfer rate. *Journal of Geophysical Research*, *113*, A07309. https://doi.org/10.1029/2007JA012993

Matsuo, T., Richmond, A. D., & Hensel, K. (2003). High-latitude ionospheric electric field variability and electric potential derived from DE-2 plasma drift measurements: Dependence on IMF and dipole tilt. *Journal of Geophysical Research*, *108*(A1), 1005. https://doi.org/10.1029/2002JA009429

Mikkelsen, I. S., Jørgensen, T. S., Kelley, M. C., Larsen, M. F., Pereira, E., & Vickrey, J. (1981). Neutral winds and electric fields in the dusk auroral oval 1. Measurements. *Journal of Geophysical Research*, *86*(A3), 1513. https://doi.org/10.1029/JA086iA03p01513

Newell, P. T., Sotirelis, T., & Wing, S. (2009). Diffuse, monoenergetic, and broadband aurora: The global precipitation budget. *Journal of Geophysical Research*, *114*, A09207. https://doi.org/10.1029/2009JA014326

Paxton, L. J., Meng, C.-I., Fountain, G. H., Ogorzalek, B. S., Darlington, E. H., Gary, S. A., et al. (1992). Special sensor ultraviolet spectrographic imager: An instrument description, Proceedings SPIE 1745, Instrumentation for Planetary and Terrestrial Atmospheric Remote Sensing. https://doi.org/10.1117/12.60595

Picone, J. M., Hedin, A. E., Drob, D. P., & Aikin, A. C. (2002). NRLMSISE-00 empirical model of the atmosphere: Statistical comparisons and scientific issues. *Journal of Geophysical Research*, *107*(A12), 1468. https://doi.org/10.1029/2002JA009430

Qian, L., Burns, A. G., Emery, B. A., Foster, B., Lu, G., Maute, A., et al. (2014). *The NCAR TIE-GCM: A Community Model of the Coupled Thermosphere/Ionosphere Syst*, *Geophysical MonographSeries*. American Geophysical Union. https://doi.org/10.1002/9781118704417.ch7

Rees, M. H., & Luckey, D. (1974). Auroral electron energy derived from ratio of spectroscopic emissions 1. Model computations. *Journal of Geophysical Research*, *79*(34). https://doi.org/10.1029/JA079i034p05181

Richmond, A. D. (1992). Assimilative mapping of ionospheric electrodynamics. *Advances in Space Research*, *12*(6), 59–68. https://doi.org/10.1016/0273-1177(92)90040-5

Richmond, A. D. (1995). Ionospheric electrodynamics using magnetic apex coordinates. *Journal of Geomagnetism and Geoelectricity*, *47*(2), 191–212. https://doi.org/10.5636/jgg.47.191

Richmond, A. D., & Kamide, Y. (1988). Mapping electrodynamic features of the high-latitude ionosphere from localized observations: Technique. *Journal of Geophysical Research*, *93*(A6), 5741. https://doi.org/10.1029/JA093iA06p05741

Richmond, A. D., Ridley, E. C., & Roble, R. G. (1992). A thermosphere/ionosphere general circulation model with coupled electrodynamics. *Geophysical Research Letters*, *19*(6), 601–604. https://doi.org/10.1029/92GL00401

Richmond, A. D., & Thayer, J. P. (2000). Ionospheric Electrodynamics: A Tutorial. *In Magnetospheric Current Systems*, *Geophysical Monograph Series*. American Geophysical Union. https://doi.org/10.1029/GM118p0131

Ridley, A. J., Lu, G., Clauer, C. R., & Papitashvili, V. O. (1998). A statistical study of the ionospheric convection response to changing interplanetary magnetic field conditions using the assimilative mapping of ionospheric electrodynamics technique. *Journal of Geophysical Research*, *103*(A3), 4023–4039. https://doi.org/10.1029/97JA03328

Robinson, R. M., & Vondrak, R. R. (1985). Characteristics and sources of ionization in the continuous aurora. *Radio Science*, *20*(3), 447–455. https://doi.org/10.1029/RS020i003p00447

Roble, R. G., & Ridley, E. C. (1987). An auroral model for the NCAR thermospheric general circulation model (TGCM). *Annales Geophysicae Series A-upper Atmosphere and Space Sciences*, *5*(6). http://n2t.net/ark:/85065/d70v8ckz

Roble, R. G., & Ridley, E. C. (1994). A thermosphere-ionosphere-mesosphere-electrodynamics general circulation model (time-GCM): Equinox solar cycle minimum simulations (30–500 km). *Geophysical Research Letters*, *21*(6), 417–420. https://doi.org/10.1029/93GL03391

Roble, R. G., Ridley, E. C., & Dickinson, R. E. (1987). On the global mean structure of the thermosphere. *Journal of Geophysical Research*, *92*(A8), 8745. https://doi.org/10.1029/JA092iA08p08745

Roble, R. G., Ridley, E. C., Richmond, A. D., & Dickinson, R. E. (1988). A coupled thermosphere/ionosphere general circulation model. *Geophysical Research Letters*, *15*(12), 1325–1328. https://doi.org/10.1029/GL015i012p01325

Shapiro, R. (1970). Smoothing, filtering, and boundary effects. *Reviews of Geophysics*, *8*(2), 359. https://doi.org/10.1029/RG008i002p00359

Shim, J. S., Kuznetsova, M., Rastätter, L., Bilitza, D., Butala, M., Codrescu, M., et al. (2012). CEDAR electrodynamics thermosphere ionosphere (ETI) challenge for systematic assessment of ionosphere/thermosphere models: Electron density, neutral density, *NmF*2, and *hmF*2 using space based observations. *Space Weather*, *10*, S10004. https://doi.org/10.1029/2012SW000851

Sutton, E. K., Forbes, J. M., & Nerem, R. S. (2005). Global thermospheric neutral density and wind response to the severe 2003 geomagnetic storms from CHAMP accelerometer data. *Journal of Geophysical Research*, *110*, A09S40. https://doi.org/10.1029/2004JA010985

Thayer, J. P., & Semeter, J. (2004). The convergence of magnetospheric energy flux in the polar atmosphere. *Journal of Atmospheric and Solar-Terrestrial Physics*, *66*(10), 807–824. https://doi.org/10.1016/j.jastp.2004.01.035

Thayer, J. P., Vickrey, J. F., Heelis, R. A., & Gary, J. B. (1995). Interpretation and modeling of the high-latitude electromagnetic energy flux. *Journal of Geophysical Research*, *100*(A10), 19715. https://doi.org/10.1029/95JA01159

Wang, W., Burns, A. G., Solomon, S., & Killeen, T. L. (2005). High-resolution, coupled thermosphere-ionosphere models for space weather applications. *Advances in Space Research*, *36*(12), 2486–2491. https://doi.org/10.1016/j.asr.2003.11.025

Weimer, D. R. (2005). Improved ionospheric electrodynamic models and application to calculating Joule heating rates. *Journal of Geophysical Research*, *110*, A05306. https://doi.org/10.1029/2004JA010884

Wu, Q., Ortland, D. A., Foster, B., & Roble, R. G. (2012). Simulation of nonmigrating tide influences on the thermosphere and ionosphere with a TIMED data driven TIEGCM. *Journal of Atmospheric and Solar-Terrestrial Physics*, *90-91*(61–67), 61–67. https://doi.org/10.1016/j.jastp.2012.02.009

Yamazaki, Y., Richmond, A. D., Maute, A., Wu, Q., Ortland, D. A., Yoshikawa, A., et al. (2014). Ground magnetic effects of the equatorial electrojet simulated by the TIE-GCM driven by TIMED satellite data. *Journal of Geophysical Research: Space Physics*, *119*, 3150–3161. https://doi.org/10.1002/2013JA019487

Yuan, T., Zhang, Y., Cai, X., She, C.-Y., & Paxton, L. J. (2015). Impacts of CME-induced geomagnetic storms on the midlatitude mesosphere and lower thermosphere observed by a sodium lidar and TIMED/GUVI. *Geophysical Research Letters*, *42*, 7295–7302. https://doi.org/10.1002/2015GL064860

Zhu, Q., Deng, Y., Richmond, A., & Maute, A. (2018). Small-scale and mesoscale variabilities in the electric field and particle precipitation and their impacts on Joule heating. *Journal of Geophysical Research: Space Physics*, *123*, 9862–9872. https://doi.org/10.1029/2018JA025771

Zhu, Q., Deng, Y., Richmond, A., Maute, A., Chen, Y., Hairston, M., et al. (2020). Impacts of binning methods on high-latitude electrodynamic forcing: Static versus boundary-oriented binning methods. *Journal of Geophysical Research: Space Physics*, *125*, e2019JA027270. https://doi.org/10.1029/2019JA027270